Earth-Science Reviews 263 (2025) 105073

Contents lists available at ScienceDirect

Earth-Science Reviews

journal homepage: www.elsevier.com/locate/earscirev

A review and discussion on the influences of grain-coating clay minerals on water-rock interactions in sandstones

Huan Li [a,b,c,*], Qinhong Hu [c,d,**], Stuart Jones [e], Jon Gluyas [e], Eric O. Ansah [b,f], Saju Menacherry [g], Qiqi Wang [h], Tao Ye [i]

[a] School of Geosciences, Yangtze University, Wuhan 430100, China
[b] School of Geography, Earth and Atmospheric Sciences, The University of Melbourne, VIC 3010, Australia
[c] National Key Laboratory of Deep Oil and Gas, China University of Petroleum (East China), Qingdao 266580, China
[d] Laboratory for Marine Mineral Resource, Qingdao Marine Science and Technology Center, Qingdao 266237, China
[e] Department of Earth Sciences, Durham University, Durham DH1 3LE, UK
[f] WH Bryan Mining & Geology Research Centre, Sustainable Minerals Institute, University of Queensland, Brisbane 4072, Australia
[g] Australian School of Petroleum and Energy Resources, University of Adelaide, Adelaide, Australia
[h] Bureau of Economic Geology, The University of Texas at Austin, Austin, TX 78758, USA
[i] Institute of Sedimentary Geology, Chengdu University of Technology, Chengdu 610059, China

ARTICLE INFO

Keywords:
Grain-coating clay
Water-rock interaction
Surface area
Mineral dissolution kinetics
Coupled dissolution-precipitation
Quartz cement

ABSTRACT

This work reviews the current understanding and challenges in evaluating the influences of grain-coating clay minerals on water-rock interactions in sandstones. Subsequently, mathematical formulations and reactive transport modelling were employed to advance the understanding of clay coats. Firstly, clay coats can reduce the accessible surface area of detrital grains, which is collectively controlled by the coat coverage, clay platelet thickness, and the width of gap between neighbouring clay platelets. Nevertheless, an extensive coat coverage does not necessarily lead to a significant decrease in the accessible surface area of detrital grains. Secondly, clay coats can retard the diffusion of ions and molecules passing through the coating layer, which is jointly controlled by the microporosity, tortuosity, and thickness of the coating layer. These two effects may significantly decelerate the dissolution rate of detrital reactive grains being coated (e.g., feldspars) and inhibit the precipitation of secondary quartz. Furthermore, the inhibition of secondary quartz by clay coats is also significantly controlled by the width of gap between neighbouring clay platelets and the solid barrier created by clay platelets themselves. Moreover, although the identification and quantification remain challenging, clay coats may undergo a significant dissolution. As a result, the reactivity and compositions of clay coats may significantly impact mineral dissolution and precipitation and sandstone porosity. This study, for the first time, integrates the multiple roles of clay coats in water-rock interactions in sandstones and may serve as a reference for analyzing the influences of clay coats on sandstone diagenesis and geological gas storage.

1. Introduction

A variety of grain-coating minerals in sandstones have been documented, such as clay minerals (Walderhaug and Porten, 2022), oxides (Wigley et al., 2012), and carbonates (Virolle et al., 2022), while this study mainly discusses broadly grain-coating clay minerals in all geochemical settings. Reported grain-coating clay minerals involve chlorite (Worden et al., 2020), smectite (Tang et al., 2018), kaolinite (Waldmann and Gaupp, 2016), illite (Freiburg et al., 2022; Bello et al., 2023), and various detrital clays (Walderhaug and Porten, 2022). The widespread interests in grain-coating clay minerals are mainly due to (1) their unique roles as indicators of sedimentary environments, where grain-coating clays are most frequently found in estuarine and deltaic settings (Dowey et al., 2012; Worden et al., 2020), and (2) their influences on inhibiting quartz cements and preserving deeply-buried sandstone porosity (Heald and Anderegg, 1960; Cecil and Heald, 1971; Heald and Larese, 1974; Ehrenberg, 1993; Lander and Walderhaug, 1999; Bloch et al., 2002; Ajdukiewicz and Larese, 2012; Worden

* Corresponding author at: School of Geosciences, Yangtze University, Wuhan 430100, China.
** Corresponding auhtor at: National Key Laboratory of Deep Oil and Gas, China University of Petroleum (East China), Qingdao 266580, China
E-mail addresses: lihuantry@yangtzeu.edu.cn (H. Li), huqinhong@upc.edu.cn (Q. Hu).

https://doi.org/10.1016/j.earscirev.2025.105073
Received 24 October 2024; Received in revised form 10 January 2025; Accepted 18 February 2025
Available online 21 February 2025

et al., 2020; Walderhaug and Porten, 2022; Gong et al., 2023). The sedimentary controls on the development of grain-coating clay minerals have been extensively discussed in both modern (Griffiths et al., 2018; Wooldridge et al., 2019) and ancient environments (Bartier et al., 1998; Gould et al., 2010; Morad et al., 2010; Saïag et al., 2016; Azzam et al., 2023; Akinlotan et al., 2024), which are not the focus of this study. Instead, this study delves into the diverse roles of grain-coating clay minerals in mineral dissolution and precipitation (water-rock interactions) in sandstones.

The formation of grain-coating clay minerals can originate through either detrital or diagenetic processes. Detrital grain-coating clay minerals may adhere to grain surfaces through the infiltration of clay particles into sandstone or the mechanical accretion of clay particles onto grain surfaces as grains roll (Aagaard et al., 2000; Bahlis and De Ros, 2013; Beaufort et al., 2015; Worden et al., 2020). The attachment of clay minerals onto detrital grains may be facilitated by multiple binding agents, such as biofilms (Wooldridge et al., 2017; Duteil et al., 2020; Charlaftis et al., 2023), metal oxides, and organic matter (Haile et al., 2022). However, these binding agents are not essential, as suspended clays can directly attach onto grain surfaces (Haile et al., 2015, 2022). Diagenetic grain-coating clay minerals involve the following two pathways: (1) Clay coats can directly precipitate on grain surfaces from clay-supersaturated pore waters (Worden et al., 2020; Charlaftis et al., 2021; Haile et al., 2022), and materials for clay growth can be derived from multiple sources, such as volcanic rock fragments, heavy minerals, biotite, and carbonates (e.g., siderite) (Berger et al., 2009; Bahlis and De Ros, 2013; Worden et al., 2020; Lin et al., 2023); (2) One precursor grain-coating clay mineral may diagenetically transform into another, such as the transformation of precursor smectite or berthierine coats into chlorite coats (Hillier, 1994; Anjos et al., 2003; Beaufort et al., 2015; Worden et al., 2020) and the transformation of chlorite coats into kaolinite coats (Waldmann and Gaupp, 2016).

In the context of water-rock interactions, previous studies have mainly focused on elaborating and evaluating the inhibitive effects of clay coats on the precipitation of secondary quartz cements on the surface of detrital quartz, which has been widely recognized as a vital factor in preserving deeply-buried sandstone porosity (Cecil and Heald, 1971; Lander and Walderhaug, 1999; Ajdukiewicz and Larese, 2012; Worden et al., 2020; Walderhaug and Porten, 2022). In general, it has been suggested that clay coats can reduce the available surface area of detrital quartz and therefore inhibit the growth of quartz cements (Lander and Walderhaug, 1999; Ajdukiewicz and Larese, 2012; Worden et al., 2020; Walderhaug and Porten, 2022). However, how clay coats reduce the surface area of detrital grains is not well understood and the quantitative mechanisms are not well established at present. Moreover, the efficiency of grain-coating clays on inhibiting quartz cements may depend on (1) multiple coat parameters, such as coat coverage (Lander and Walderhaug, 1999; Taylor et al., 2010; Ajdukiewicz and Larese, 2012) and coat thickness (Griffiths et al., 2021; Hansen et al., 2021), and (2) other factors that may impact the precipitation kinetics of quartz, such as temperature (Dong et al., 2024; Lander et al., 2022; Taylor et al., 2022).

Moreover, since clay coats can grow on the surface of any detrital grains (Worden et al., 2020; Griffiths et al., 2021), clay coats could also reduce the accessible surface area of other detrital reactive grains such as feldspars. However, the potential influence of grain-coating clays on the dissolution of these detrital reactive grains receives less attention. Additionally, previous studies often treat clay coats as relatively chemically-stable minerals. The potential dissolution of clay coats is usually neglected. While a few case studies have supported the feasibility of the dissolution of clay coats (Higgs et al., 2015; Waldmann and Gaupp, 2016; Li et al., 2024a), the influence of the dissolution of clay coats on water-rock interactions in sandstones remains largely underexplored.

Therefore, this study reviews and discusses the current understanding and challenges associated with evaluating the various roles of grain-coating clays in water-rock interactions in sandstones, including their roles in reducing the surface area of detrital grains, retarding the diffusion of molecules and ions passing through the coating layer, decelerating the dissolution rate of detrital reactive grains being coated and inhibiting quartz overgrowth, and the influence of the dissolution of clay coats. The objective is to offer a comprehensive reference for future investigations into grain-coating clays in sandstones.

2. Reduction in the accessible surface area of detrital grains by clay coats

2.1. Current knowledge

The definitions of mathematical symbols used in this study are compiled in Table 1. A key factor that controls the dissolution and precipitation rates of minerals is the accessible surface area (*ASA*) of the mineral, as demonstrated in the kinetic equation constraining mineral dissolution (Eq. 1; Lasaga, 1998). The accessible surface area is defined as the mineral surfaces in contact with connected pore spaces (Peters, 2009; Landrot et al., 2012).

$$Rate = ASA \times k \times e^{\frac{-E_A}{RT}} \times \prod_i a_i^{n_i} g(I) \times f(\Delta G) \quad (1)$$

Table 1
Nomenclature of mathematical symbols used in this study.

Symbol	Description
ASA	Accessible surface area (mm^2)
a_i	Activity of the inhibiting or promoting species i
C	Coating factor, coat coverage (%)
d	Grain size (mm)
D_i	Diffusion coefficient of the species i in free solution (cm^2/s)
D_i^{eff}	Effective diffusion coefficient of the species i in a porous media (cm^2/s)
E_A	Activation energy (J/mol)
$f(\Delta G)$	A term describing a reaction approaching equilibrium and is a function of the saturation state
$g(I)$	A term describing ionic strength dependencies
k	Rate constant at standard conditions ($mol/cm^2/s$)
k_p	Proportionality factor
K	Equilibrium constant
l	Coating layer thickness
m, n	Empirical and dimensionless orders of the rate law
n_i	Reaction orders with respect to the species i
p	Sphericity factor related to the grain shape
Q	Activity product
$Rate$	Mineral dissolution or precipitation rate (mol/s)
R	Gas constant
r	Grain radius (mm)
SSA	Specific surface area (mm^{-1})
S	Surface area of a free sphere (mm^2)
S_a	Available surface area (mm^2)
S_i	Concentration of the dissolved species i (mol/L)
$SA_{(t)}$	Surface area of primary mineral at time t (mm^2)
$SSA_{(0)}$	Initial specific surface area of primary mineral (mm^{-1})
S_c	Solubility of a small quartz crystal (mol/L)
S_0	Solubility of a quartz crystal of infinite size (mol/L)
T	Temperature (°C)
t_c	Thickness of a single clay platelet (μm)
t	Time (s)
$V_{primary(0)}$	Initial volume of primary mineral (cm^3)
$V_{secondary(t)}$	The volume of secondary phase at time t (cm^3)
V_m	Molar volume of quartz (cm^3/mol)
ν	Moles of silica produced by the dissolution of one mole of quartz (mol)
w_g	The width of a gap between neighbouring individual clay platelet (μm)
x	Distance (μm)
β	The proportion of the surface area that is occupied by other detrital grains and cements other than quartz (%)
γ	Mineral-water interfacial free energy (J/m^2)
Ω	The ratio of clay platelet thickness over gap width
ε	Ratio of porosity (ϕ) over tortuosity (τ) of the porous layer
ϕ	Porosity of the coating layer (%)
τ	Tortuosity of the porous coating layer

where *Rate* represents mineral dissolution rate, k is the rate constant at standard conditions, E_A is activation energy, R is gas constant, T is temperature in Kelvin, a_i is the activity of the inhibiting or promoting species i, n_i is the reaction orders with respect to the species i, $g(I)$ is the a term describing ionic strength dependencies, and $f(\Delta G)$ describes reaction approaching equilibrium and is a function of the saturation state.

Previous studies have suggested that grain-coating clays can occupy a part of the surface area of detrital grains and employed Eq. 2 to achieve the inhibitive influence of grain coats on the growth of quartz cements (Eq. 2; Lander and Walderhaug, 1999; Walderhaug et al., 2000; Lander et al., 2022). The construction of this equation is mainly based on the petrographic observation, where visible quartz overgrowths in thin sections and low-resolution scanning electron microscopy (SEM) images can only be observed at coat breaks (Figs. 1A–B; Bloch et al., 2002; Ajdukiewicz and Larese, 2012; Walderhaug and Porten, 2022). Therefore, it is assumed that only the surface area of detrital quartz uncoated with clays is accessible for the quartz precipitation (Lander and Walderhaug, 1999; Walderhaug et al., 2000; Lander et al., 2022).

$$ASA\ of\ detrital\ quartz = (1 - C) \times SSA \tag{2}$$

where C is the coating factor, which is equivalent to the coat coverage. Coat coverage is defined as the fraction of detrital grain surface area covered by clay minerals and typically measured in 2D petrographic images (Franks and Pantano, 2021; Taylor et al., 2022). *SSA* is the specific surface area of coat-free detrital quartz.

However, grain-coating clays are typically porous and have varying proportions of intergranular microporosity or gaps among individual clay crystals (Figs. 1C–D; Table 2; Hurst and Nadeau, 1995; Alansari et al., 2019; Xia et al., 2020; Giannetta et al., 2021). These micropores or gaps generally have sizes of up to a few microns (Xia et al., 2020; Giannetta et al., 2021; Walderhaug and Porten, 2022). For example, Walderhaug and Porten (2022) measured the widths of gaps between neighbouring individual grain-coating clay platelets attached on the surface of detrital grains, including chlorite, illite, kaolinite, and detrital clay, from eight sandstone datasets in the Norwegian continental shelf. The measured gap width ranges from 0.3 μm to 7 μm (Walderhaug and Porten, 2022).

Theoretically, this porous attribute can allow water molecules and dissolved species to traverse the coating layer because the diameters of water molecules and dissolved species typically fall within the nanometre scale (Walderhaug and Porten, 2022). Two petrographic observations support this hypothesis. Firstly, numerous case studies have observed the presence of very tiny secondary quartz crystals (anhedral or euhedral) beneath the coating layer or situated in between neighbouring individual clay platelets (Figs. 1C–D; Table 3). In a section across clay coats and detrital quartz, it appears that the clay platelets grow, or insert, into the detrital quartz grain (Figs. 1C–D; Storvoll et al., 2002; Billault et al., 2003; Walderhaug and Porten, 2022). Secondly, numerous case studies have observed a unique phenomenon where feldspar grains being coated are either partially or completely dissolved, while the grain-coating clays maintain original detrital grain shapes (Figs. 1E–F; Storvoll et al., 2002; Ajdukiewicz and Lander, 2010; Taylor et al., 2015; Walderhaug and Porten, 2022; Li et al., 2023a). This observation supports the assertion that undersaturated pore waters can penetrate the coating layer and react with the feldspar grains being coated. Therefore, it is not correct to assume that the surface area of a detrital grain coated with clays is completely inaccessible to pore water as employed in Eq. 2 (Lander and Walderhaug, 1999; Walderhaug et al., 2000).

However, one critical uncertainty is to what extent do grain-coating clays scale down the accessible surface area of detrital grains. While studies by Zerai et al. (2006) and Xu et al. (2007) did not directly measure the surface area of clay-coated detrital grains, both introduced a scaling factor of 10^{-2} to address the reduction in the surface area of detrital grains caused by clay coats. The only experimental study addressing the influence of clay coats on the reduction of the surface area of detrital grains was conducted by Peters (2009), who utilized 2D high-resolution BSEM images to assess the accessible surface area of kaolinite-coated sandstones from the Cretaceous Viking Formation, Albert Basin, Canada. Peters (2009) suggested that only one-third of the minerals were connected with pore spaces (i.e., accessible surface area) due to kaolinite coats. However, the coat coverage was not measured, though BSEM images likely indicated a high coat coverage (>80 %). Furthermore, no mathematical correlation between the accessible surface areas of detrital grains and clay coat parameters (e.g., coat coverage) was established. Nevertheless, the study of Peters (2009) likely suggests that grain-coating kaolinite with a high coat coverage (>80 %) can reduce the accessible surface area of detrital grains by one order of magnitude.

In comparison, Waldmann et al. (2014) employed a geometric method to evaluate the accessible surface area of kaolinite-coated sandstones from the Permian Slochteren Formation, Southern Permian Basin, NE Netherlands. In their study, grain-coating kaolinite was assumed to be perpendicular to detrital grains and possessed an ideal hexagonal crystal structure. Moreover, detrital quartz grains were assumed to be spheres. Although coat coverage was not reported in Waldmann et al. (2014), another study by these authors discussing the formation mechanism of grain-coating kaolinite in the same sample dataset indicated a high coat coverage (>80 %), albeit without precise measurements (Waldmann and Gaupp, 2016). The derived geometric accessible surface area of detrital quartz is 0.01 m^2/g (mean value) (Waldmann et al., 2014). Compared with the reported ranges of BET (Brunauer-Emmett-Teller) surface area of unconsolidated quartz grains (0.0225–0.111 m^2/g; Brady and Walther, 1990; Tester et al., 1994; Beckingham et al., 2016) and high-resolution image-derived surface area of detrital quartz in consolidated sandstones (0.089 m^2/g; Beckingham et al., 2016, 2017), it is likely that the surface area of detrital quartz in the study by Waldmann et al. (2014) may be reduced by up to one order of magnitude.

2.2. A new geometric estimation

In this study, we employed a geometric method to roughly estimate the influence of clay coats on the reduction of accessible surface area of detrital grains (Fig. 2). As a simplification of the mathematical formalism, the grain-coating clay platelets are hypothesized to be perpendicular to the grain surface and evenly distributed on the detrital grain surface. Detrital grains were assumed to be spheres with an equal diameter (Fig. 2A). The surface area of a single sphere without the presence of clay coats, grain contacts, and other cements can be calculated as:

$$S = 4\pi r^2 = 4\pi\left(\frac{d}{2}\right)^2 \tag{3}$$

where S is the surface area of a free sphere (mm^2), r is the grain radius (mm), and d is grain size (mm).

Other factors, such as mechanical compaction and early diagenetic cements other than quartz, may result in the reduction of accessible surface area of detrital grains (e.g., Figs. 1E and 2A–B; Waldmann et al., 2014; Qin et al., 2023; Li et al., 2024a). The surface area of detrital grains occupied by other detrital grains, which is induced by mechanical compaction (Figs. 1E and 2A–B), and by cements other than quartz (Figs. 2A–B) can be defined as the unavailable surface area (Fig. 2B; Franks and Pantano, 2021; Taylor et al., 2022). In comparison, the surface area of detrital grains that is not occupied by other detrital grains and cements other than quartz can be defined as the available surface area (Fig. 2B; Franks and Pantano, 2021; Taylor et al., 2022). The definitions of available and unavailable surface areas refer to the quantification of clay coat coverage (Franks and Pantano, 2021; Taylor et al., 2022). Thus, a factor (β) is introduced to account for the unavailable

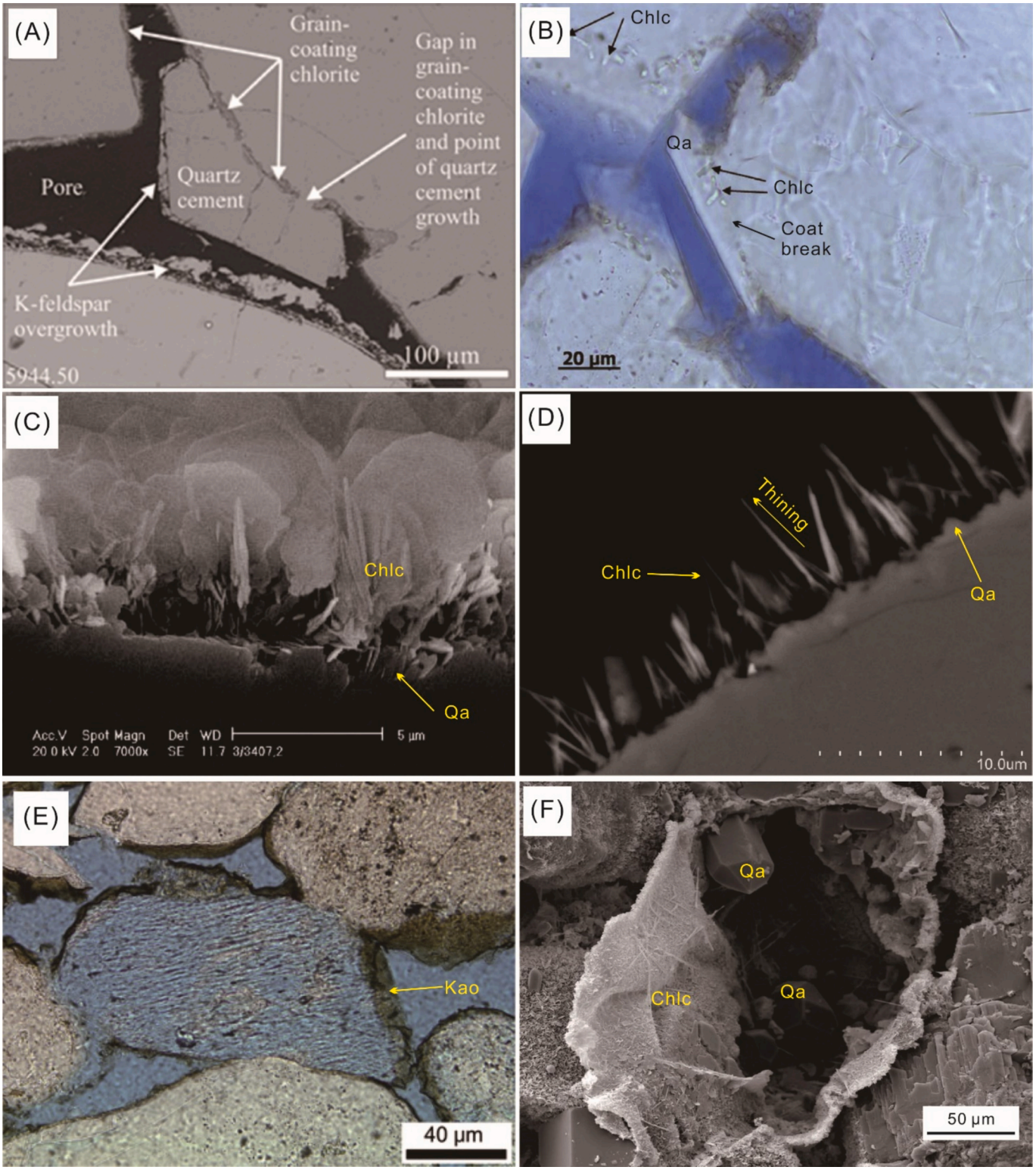

Fig. 1. (A–B) A large quartz overgrowth (Qa) grows at a small chlorite coat (Chlc) break (A from Griffiths et al., 2021; B from Taylor et al., 2015). Moreover, two individual chlorite platelets are incorporated into the quartz overgrowth in the panel B. (C—D) Grain-coating chlorite and tiny quartz crystals grown in between individual chlorite platelets (A from Berger et al., 2009; B from Walderhaug and Porten, 2022). Chlorite platelets appear to insert into the detrital quartz grain. Note the decreasing thickness of a single platelet towards pore space in the Panel B. (E–F) Detrital grains being coated are dissolved, whereas the grain-coating kaolinite (Kao) and chlorite maintain the original feldspar grain shapes (C from Waldmann and Gaupp, 2016; D from Li et al., 2023a).

Table 2
Reported microporosity values of clay minerals in sandstones.

Clays	Texture	Microporosity (%)		Means[a]	References
		Range	Mean/ average		
Kaolinite	Vermicular	40–61	43	BSEM	Hurst and Nadeau (1995)
	Blocky	15–30			
	Booklet	35–55	45	SEM	Alansari et al. (2019)
	Booklet	35–60	46	BSEM	Giannetta et al. (2021)
	Blocky	18–34	26		
	Vermicular	45–50	48		
Chlorite	Grain-coating	44–58	51	BSEM	Hurst and Nadeau (1995)
	Grain-coating	15–35	20	SEM	Alansari et al. (2019)
	Rims	39–56	50	BSEM	Giannetta et al. (2021)
	Clusters	65–80	72		
Illite	Fibrous	47–76	63	BSEM	Hurst and Nadeau (1995)
	Grain-coating; bridging	30–50	35	SEM	Alansari et al. (2019)
	Hairs	59–65	61	BSEM	Giannetta et al. (2021)
	Mats	63–70	67		
Smectite	Grain-coating	10–35	15	SEM	Alansari et al. (2019)
	Webs	65	65	BSEM	Giannetta et al. (2021)

[a] BSEM: backscattered scanning electron microscopy; SEM: scanning electron microscopy.

surface area (Li et al., 2024a) as follows:

$$S_a = S \times (1-\beta) = 4\pi\left(\frac{d}{2}\right)^2 \times (1-\beta) \quad (4)$$

where S_a is the available surface area (mm^2) and β represents the proportion of the surface area that is occupied by other detrital grains and cements other than quartz and theoretically ranges from 0 to 1.

Furthermore, the available surface area for a clay-coated grain can be divided into two segments, including a coated segment and an uncoated segment (Fig. 2B; Franks and Pantano, 2021; Taylor et al., 2022). The uncoated segment represents coat breaks (Fig. 2B). Therefore, the entire surface area at the uncoated segment is accessible for pore water. The surface area at the uncoated segment can be calculated as follows:

$$\textit{surface area at the uncoated segment} = S_a \times (1-C) = 4\pi\left(\frac{d}{2}\right)^2 \times (1-\beta) \times (1-C) \quad (5)$$

where C is the coat coverage.

It is important to note that the measurement of coat coverage excludes the unavailable surface area that is occupied by other detrital grains and cements other than quartz (Fig. 2B; Franks and Pantano, 2021; Taylor et al., 2022). Assuming no coats or coats removed, the surface area at the coated segment can be calculated as follows:

$$\textit{surface area at coated segment with coats removed} = S_a \times C = 4\pi\left(\frac{d}{2}\right)^2 \times (1-\beta) \times C \quad (6)$$

The coated segment can be further divided into two parts (Figs. 2B–C), including clay platelets and gaps between neighbouring individual clay platelets. In this study, clay platelets were assumed to be evenly distributed on the surface of detrital grains, resulting in an equal clay platelet thickness and an equal gap width (Figs. 2B–C). The part occupied by clay platelets is not accessible for pore water. In comparison, the surface areas at gaps are not occupied by any minerals or phases and therefore accessible for pore water (Figs. 2B–C). In this way, only the surface area directly occupied by clay platelets should be counted to estimate the reduction of accessible surface area of detrital grains caused by clay coats. Therefore, the total accessible surface area of a clay-coated grain sphere can be calculated as follows:

$$\text{total accessible surface area of a clay coated grain sphere} = \text{surface areas at the uncoated segment} + \text{surface areas at gaps} \quad (7)$$

In this study, we used a 2D section of a clay-coated detrital quartz grain to estimate the proportion of the surface area occupied by clay platelets and the proportion of surface area at gaps. In a section of a detrital grain sphere, the perimeter of the available surface can be calculated as follows:

$$\textit{perimeter of available surface} = 2\pi r^2 \times (1-\beta) = 2\pi\left(\frac{d}{2}\right)^2 \times (1-\beta) \quad (8)$$

Furthermore, in the available surface, the perimeter of the coated segment is calculated as follows:

Table 3
Reported clay-coated sandstones in which microquartz crystals were observed beneath clay coats or within micropores of clay coats.

Location	Age	Formation	Sedimentary environment	Depth (m)	Temperature (°C)	Grain coating mineralogy	Microquartz presence	References
Norway	Jurassic	Haltenbanken reservoir	Shallow marine deltaic	4443	180	Chlorite	✓	Billault et al. (2003)
Oman	Permian	Malih Xl reservoir	Marine fluvial	4003.6	130	Chlorite	✓	
Pakistani Sawan gas field	Cretaceous	Lower Goru Fm.	Shallow marine deltaic	3407.2	164	Chlorite	✓	Berger et al. (2009)
Louisiana, USA	Cretaceous	Tuscaloosa Fm.	Fluvial-deltaic	5043.07	164	Chlorite	✓	Ajdukiewicz and Lander (2010)
	Cretaceous	Tuscaloosa Fm.	Fluvial-deltaic	5503.77	170	Chlorite	✓	
Paris Basin, France	Cretaceous	Wealden Group	Marine coastal estuarine	~950	~37	Berthierine	✓	Virolle et al. (2022)
Norwegian continental shelf	Lower Jurassic	Tilje Fm.	Marginal marine	5242.75	162	Chlorite	✓	Walderhaug and Porten (2022)
	Permian	Rotligend Group	Eolian	5123	165	Illite	✓	
	Triassic	Lomvi Fm.	Fluvial	4146.5	147	Illite	✓	
	Triassic	Lomvi Fm.	Fluvial	4147.75	147	Illite	✓	
	Upper Cretaceous	Springar Fm.	Turbiditic	3263	96	Mixed illite, kaolin and chlorite	✓	
	Upper Jurassic	Draupne Fm.	Turbiditic	4302.3	138	Microcrystalline quartz	✓	

$$\begin{aligned} \textit{perimeter of coated segment} &= \textit{perimeter of available surface} \times C \\ &= 2\pi\left(\frac{d}{2}\right)^2 \times (1-\beta) \times C \end{aligned} \tag{9}$$

The perimeter of coated segment can be alternatively calculated, considering the thickness of a clay platelet (t_c) and the width of a gap (w_g), as follows:

$$\begin{aligned} \textit{perimeter of coated segment} &= (\textit{thickness of a single clay platelet} \\ &\quad + \textit{width of a gap}) \times \textit{number of clay platelets} \\ &= (t_c + w_g) \times \textit{number of clay platelets} \end{aligned} \tag{10}$$

Then, the number of clay platelets can be evaluated as follows:

$$\begin{aligned} \textit{number of clay platelets} &= \frac{\textit{perimeter of coated segment}}{(t_c + w_g)} \\ &= \frac{2\pi\left(\frac{d}{2}\right)^2 \times (1-\beta) \times C}{(t_c + w_g)} \end{aligned} \tag{11}$$

In the coated segment, only surfaces at gaps are accessible, while surfaces occupied by clay platelets are inaccessible. In the coated segment, the proportion of the total perimeter occupied by clay platelets can be calculated as:

$$\begin{aligned} &\textit{proportion of perimeter occupied by clay platelets} \\ &= \frac{\textit{total thickness of clay platelets}}{\textit{perimeter of available surface}} \\ &= \frac{\textit{thickness of a single clay platelet} \times \textit{number of clay platelets}}{\textit{perimeter of available surface}} \\ &= \frac{t_c \times \frac{2\pi\left(\frac{d}{2}\right)^2 \times (1-\beta) \times C}{(t_c + w_g)}}{2\pi\left(\frac{d}{2}\right)^2 \times (1-\beta)} = \frac{t_c \times C}{(t_c + w_g)} \end{aligned} \tag{12}$$

Then, the proportion of the total perimeter at gaps can be calculated as follows:

$$\begin{aligned} \textit{proportion of perimeter at gaps} &= \frac{\textit{total gaps}}{\textit{perimeter of available surface}} \\ &= \frac{\textit{width of a gap} \times \textit{number of clay platelets}}{\textit{perimeter of available surface}} \\ &= \frac{w_g \times \frac{2\pi\left(\frac{d}{2}\right)^2 \times (1-\beta) \times C}{(t_c + w_g)}}{2\pi\left(\frac{d}{2}\right)^2 \times (1-\beta)} = \frac{w_g \times C}{(t_c + w_g)} \end{aligned} \tag{13}$$

Then, the surface area occupied by clay platelets can be calculated as follows:

$$\begin{aligned} &\text{surface area occupied by clay platelets} \\ &= \textit{surface area at the coated segment with coats removed} \\ &\quad \times \textit{proportion of perimeter occupied by clay platelets} \\ &= \left[4\pi\left(\frac{d}{2}\right)^2 \times (1-\beta) \times C\right] \times \left[\frac{t_c \times C}{(t_c + w_g)}\right] \end{aligned} \tag{14}$$

Then, the surface area at gaps can be calculated as follows:

$$\begin{aligned} \text{surface area at gaps} &= \textit{surface area at coated segment with coats removed} \\ &\quad \times \textit{proportion of perimeter at gaps} \\ &= \left[4\pi\left(\frac{d}{2}\right)^2 \times (1-\beta) \times C\right] \times \left[\frac{w_g \times C}{(t_c + w_g)}\right] \end{aligned} \tag{15}$$

Then, the total accessible surface area of a clay-coated grain sphere, based on Eq. 7, can be calculated as follows:

$$\begin{aligned} &\textit{total accessible surface area of a clay coated grain} \\ &= \textit{surface area at uncoated segment} + \textit{surface area at gaps} \\ &= \left\{4\pi\left(\frac{d}{2}\right)^2 \times (1-\beta) \times (1-C)\right\} + \left\{\left[4\pi\left(\frac{d}{2}\right)^2 \times (1-\beta) \times C\right] \times \left[\frac{w_g \times C}{(t_c + w_g)}\right]\right\} \end{aligned} \tag{16}$$

Then, the extent to which clay coats scale down the accessible surface area of a detrital grain can be evaluated as follows:

$$\begin{aligned} \textit{Proportion} &= \frac{\textit{total accessible surface area of a clay coated grain}}{\textit{available surface area}\,(S_a)} \\ &= \frac{\left\{4\pi\left(\frac{d}{2}\right)^2 \times (1-\beta) \times (1-C)\right\} + \left\{\left[4\pi\left(\frac{d}{2}\right)^2 \times (1-\beta) \times C\right] \times \left[\frac{w_g \times C}{(t_c + w_g)}\right]\right\}}{4\pi\left(\frac{d}{2}\right)^2 \times (1-\beta)} \\ &\times 100\% = \left[(1-C) + \frac{w_g \times C^2}{(t_c + w_g)}\right] \times 100\%. \end{aligned} \tag{17}$$

It is demonstrated that the reduction of the accessible surface area of detrital grains caused by clay coats is collectively controlled by the coat coverage, clay platelet thickness, and gap width. Moreover, it is clear that, given a constant coat coverage and a constant gap width, the accessible surface area of clay-coated detrital grains is negatively correlated with the clay platelet thickness (Fig. 3A). Given a constant coat coverage and a constant clay platelet thickness, the accessible surface area of clay-coated detrital grains is positively correlated with the gap width (Fig. 3B). Furthermore, both the t_c and w_g have the same unit. Thus, this work introduces a new parameter (Ω) to represent the ratio of clay platelet thickness over gap width:

$$\Omega = \frac{t_c}{w_g} \tag{18}$$

Then, the Eq. 17 can be rewritten as follows:

$$\textit{Proportion} = (1-C) + \frac{w_g \times C^2}{(t_c + w_g)} = (1-C) + \frac{C^2}{1+\Omega} = \frac{1}{1+\Omega} \times C^2 - C + 1 \tag{19}$$

If the parameter, Ω, is treated as a constant, it is clear that the extent of reduction in the accessible surface area of detrital grains caused by clay coats follows a mathematical quadratic relationship with coat coverage (Fig. 3C). As the term $\frac{1}{1+\Omega}$ is always positive, the geometric parabola shape opens upward (Fig. 3C). Theoretically, the x-coordinate of the extreme point (vertex) equals $\frac{1+\Omega}{2}$ and the y-coordinate of the extreme point equals $1 - \frac{1+\Omega}{4}$. However, given that the maximum coat coverage is 1, the extreme point cannot be observed if the x-coordinate ($\frac{1+\Omega}{2}$) of the extreme point exceeds 1 (Fig. 3C). In other words, when Ω exceeds 1, i.e., t_c is greater than w_g, the extreme point cannot be observed (Fig. 3C). Alternatively, the extent of reduction in the accessible surface area of detrital grains caused by clay coats exhibits a well negative correlation with coat coverage (Fig. 3C).

To our knowledge, no studies have systematically measured both the clay platelet thickness and gap width for the same sample dataset. Alternatively, Xia et al. (2020) measured the clay platelet thickness values of chlorite coats from three sandstone datasets, including the Cretaceous, Tuscaloosa Formation, Mississippi, the Upper Jurassic, Norphlet Formation, Gulf of Mexico, and the Upper Jurassic, Dupuy Formation, Barrow Island, Australia. The single chlorite platelet

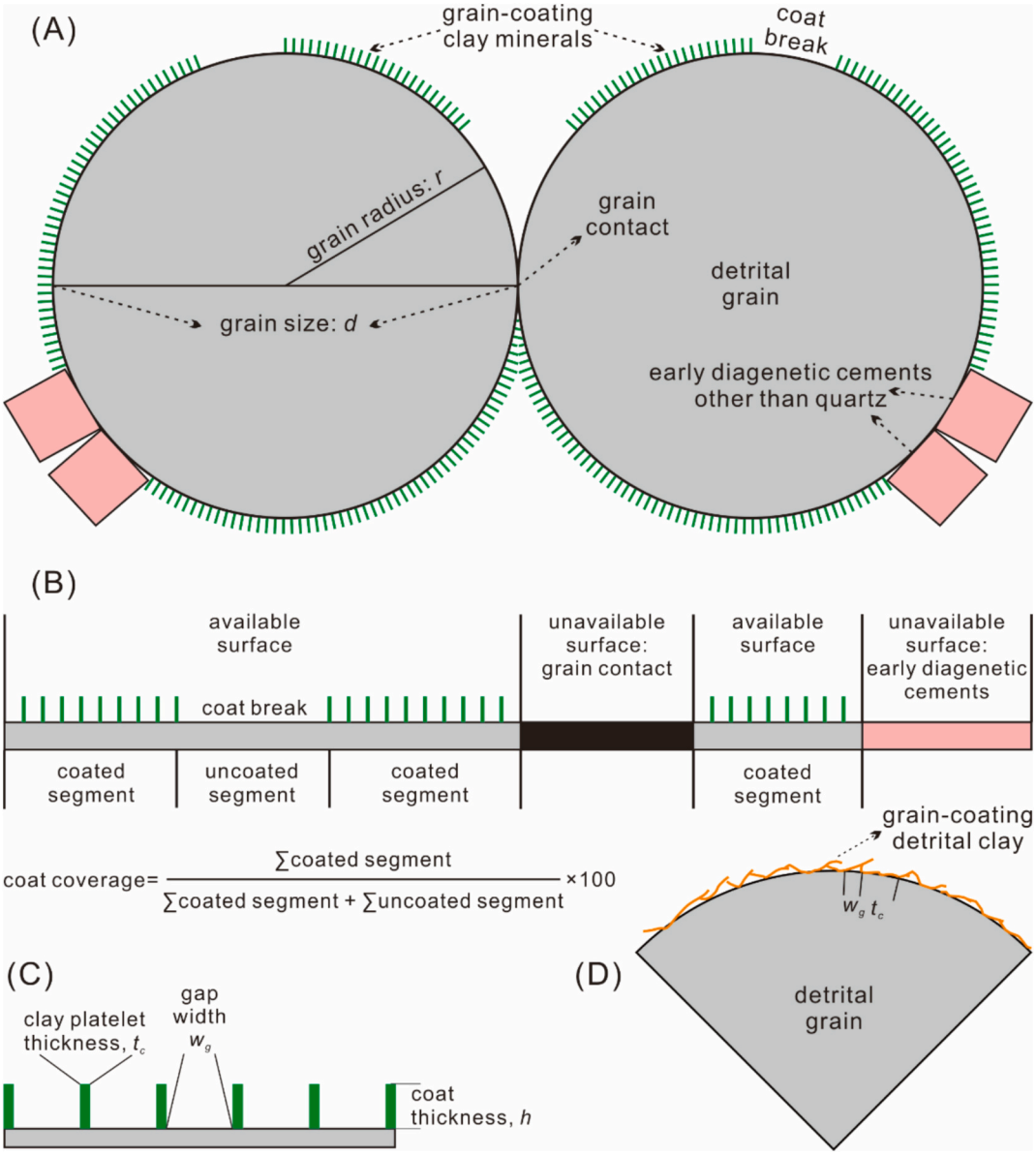

Fig. 2. (A) Schematic diagram illustrating detrital grains coated with discontinuous clay minerals; (B) Two main classifications of detrital grain surface, including the available surface and the unavailable surface; (C) Definitions of clay platelet thickness (t_c), width of the gap (w_g), and coat thickness (h); and (D) Schematic diagram illustrating grain-coating detrital clay or illite, which are typically not perpendicular to the detrital grain surface.

thickness ranges from 0.04 μm to 0.28 μm. Walderhaug and Porten (2022) measured the gap width between neighbouring individual clay platelets for various grain-coating clays, including chlorite, illite, kaolinite, and detrital clay, from eight sandstone datasets; the gap width ranges from 0.3 μm to 7 μm. Therefore, based on these two case studies, it is likely that the gap width is probably typically greater than the clay platelet thickness. If these two ranges are employed, the Ω value would range from 0.006 to 0.933. Correspondingly, it can be roughly estimated that the accessible surface area of clay-coated grains can be maximumly $(1 - \frac{1+\Omega}{4})$ reduced to 74.9 % and 51.7 % of the surface area of the counterpart coat-free grains, respectively (Eq. 19). The coat coverages corresponding to these two extreme points are 50.3 % and 96.7 %, respectively (Eq. 19). Moreover, we used the high-resolution chlorite coats shown in Fig. 1D to measure the t_c and w_g in the illustrated grain surface segment. The median values of t_c and w_g are 0.341 μm and 0.432 μm, respectively (Fig. S1 of Supplementary Material), and the calculated Ω equals 0.79. Therefore, the accessible surface area of this chlorite-coated grain segment (Fig. 1D) is reduced to 55.3 % of the surface area of the counterpart coat-free grain segment.

It is important to note that a key hypothesis underlying the aforementioned estimations is the perpendicular growth habit of clay platelets on detrital grain surfaces (Figs. 2A–C). This hypothesis is more likely reasonable for grain-coating chlorite (e.g., Figs. 1C–D; Ajdukiewicz and Larese, 2012; Worden et al., 2020; Taylor et al., 2022; Walderhaug and Porten, 2022) and kaolinite (Peters, 2009; Waldmann et al., 2014; Waldmann and Gaupp, 2016). However, grain-coating illite and detrital clay typically exhibit as flakes oriented roughly parallel to the detrital grain surface (Fig. 2D; Walderhaug and Porten, 2022). In such cases, the contact area between a clay platelet and detrital grain surface can be treated as the t_c (Fig. 2D). As a result, it is possible that t_c may be greater than w_g, resulting in a Ω value greater than 1. Then, the extreme point will not be observed. The reduction of accessible surface area of clay-coated grains will exhibit a well negative correlation with coat coverage, as illustrated in Fig. 3C. For example, given a Ω value of 2, the accessible surface area of clay-coated grains can be maximumly reduced to 33.3 % of the surface area of the counterpart coat-free grains when the

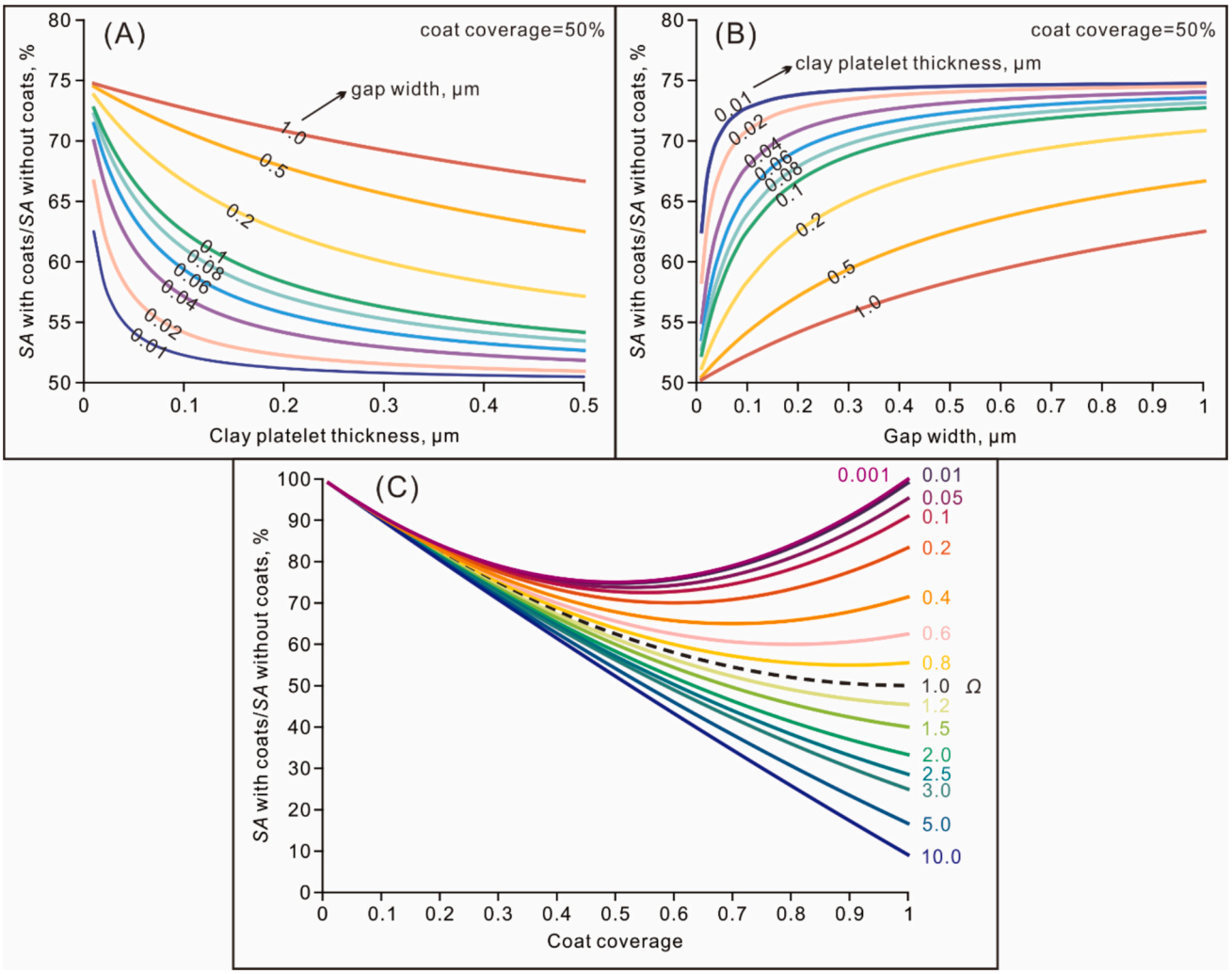

Fig. 3. (A) An example, given a coat coverage of 50 %, showing the correlation between clay platelet thickness and the reduction in accessible surface area of detrital grains with varying gap widths; (B) An example, given a coat coverage of 50 %, showing the correlation between gap width and the reduction in accessible surface area of detrital grains with varying clay platelet thicknesses; and (C) Correlation between coat coverage and the reduction in accessible surface area of detrital grains with varying ratios (Ω) of clay platelet thickness over gap width. *SA* = surface area.

coat coverage is 100 % (Fig. 3C).

In summary, the following six conclusions can be drawn: (1) The reduction of accessible surface area of detrital grains is collectively controlled by the coat coverage, clay platelet thickness (or the contact area between clay platelets and detrital grains), and gap width; (2) A higher coat coverage does not always result in a greater reduction in the accessible surface area of detrital grains; although a negative correlation between coat coverage and quartz cements is typically used to support the inhibitive effect of clay coats on quartz cements (Lander and Walderhaug, 1999; Bloch et al., 2002; Taylor et al., 2010), simply stating that clay coats inhibit quartz cements by reducing the surface area of detrital quartz is not rigorous; (3) When $w_g > t_c$, i.e., $\Omega < 1$, the reduction in the accessible surface area of detrital grains caused by clay coats exhibits a quadratic relationship with coat coverage; this scenario is more likely reasonable for grain-coating chlorite and kaolinite, which are typically perpendicular to the detrital grain surface; (4) When $w_g < t_c$, i.e., $\Omega > 1$, the reduction in the accessible surface area of detrital grains caused by clay coats demonstrates a well negative correlation with coat coverage; this scenario is more likely reasonable for grain-coating detrital clay and illite, which are usually not perpendicular to the detrital grain surface; (5) Regardless of clay mineralogy and morphology, the maximum reduction in the accessible surface area of detrital grains is consistently smaller than coat coverage; and (6) More importantly, it is highly likely that the commonly observed grain-coating clays can scale down the accessible surface area of detrital grains by up to one order of magnitude; this conclusion is consistent with the experimental results from Peters (2009) and geometric estimations from Waldmann et al. (2014).

3. Retard of mass diffusion passing through the coating layer

3.1. General background

Analogous to other minerals (Oelkers et al., 2000; Bethke, 2008; Lasaga, 2014), both the precipitation of secondary minerals (e.g., quartz) on the surface of clay-coated detrital grains and the dissolution of detrital reactive grains (e.g., feldspars) being coated should theoretically involve three major steps: (1) the diffusion of dissolved species (e.g., H^+ and SiO_2) in free fluids passing through the coating layer to arrive at the surface of detrital grains; (2) the adsorption of dissolved species onto detrital grain surface; and (3) the creation of chemical bonds between dissolved species and elements on the mineral surface, either for sink (precipitation) or breakup (dissolution). Based on these conceptually stepwise processes, the porous attribute of the coating layer (see Section 2.1) may retard the diffusion rate of dissolved species in free pore water passing through it and thereby impact the precipitation rate

of secondary minerals or the dissolution rate of detrital reactive grains being coated. However, to our knowledge, there are no studies have specifically addressed the mass diffusion passing through grain-coating clay minerals.

3.2. A new estimation of mass diffusion reduction passing through the clay coating layer

In this section, we employed Fick's second law to provide a rough estimation of mass diffusion reduction passing through the clay coating layer. The diffusion of a dissolved component passing through a porous mineral layer, i.e., grain-coating clay minerals in this case, can be expressed as follows, based on Fick's second law (Li and Gregory, 1974; Zalc et al., 2004; Tartakovsky and Dentz, 2019; Emmanuel, 2022):

$$\frac{\partial S_i}{\partial t} = \frac{\partial\left(D_i^{eff}\frac{\partial S_i}{\partial x}\right)}{\partial x} \tag{20}$$

where S_i is the concentration of the dissolved species i, t is time, x is distance, and D_i^{eff} is the effective diffusion coefficient of the species i in a porous media, which can be estimated as follows (Tartakovsky and Dentz, 2019):

$$D_i^{eff} = \varepsilon \times D_i \tag{21}$$

where D_i is the diffusion coefficient of the species i in free solution, and ε is the ratio of porosity (ϕ) over tortuosity (τ) of the porous layer, which is defined as follows (Emmanuel, 2022):

$$\varepsilon = \frac{\phi}{\tau} \tag{22}$$

Then, the Eq. 20 can be rewritten as follows:

$$\frac{\partial S_i}{\partial t} = \frac{\partial\left(\frac{\phi}{\tau}D_i\frac{\partial S_i}{\partial x}\right)}{\partial x} \tag{23}$$

In Eq. 23, parameters x, ε, ϕ, and τ represent fundamental attributes of the coating layer. Specifically, x is equivalent to the coating layer thickness (l). The parameter ϕ is equivalent to the microporosity of the coating layer. The parameter τ can be estimated using the relationship between tortuosity and porosity of a porous media (Boudreau, 1996, 1997), as follows:

$$\tau^2 = 1 - ln(\phi^2) \tag{24}$$

As an example, we calculated the normalized diffusion of silica ($SiO_{2(aq)}$) across the coating layer relative to the diffusion of silica without a coating layer at 100 °C (Fig. 4). The diffusion coefficient of silica in free solution (D_i) at a temperature of 100 °C (5.50×10^{-5} cm^2/s; Schulz and Zabel, 2006; Park, 2014; Li et al., 2024b) was employed. This value was calculated based on the diffusion coefficient of silica in seawater at 25 °C (1.75×10^{-5} cm^2/s; Schulz and Zabel, 2006) and the temperature-adjusted diffusion coefficient estimation methods provided by Park (2014):

$$D_i = 1.0 \times 10^{-6}\left(T_c + T_f \times T\right) \tag{25}$$

where T_c and T_f denote empirical constants, and T is temperature (°C).

In the case of $SiO_{2(aq)}$, the calculated T_c is 5.00 and T_f is 0.50 (Li et al., 2024b). The results indicate a substantial decline in silica diffusion across the coating layer with decreasing coat microporosity (Fig. 4A) and increasing coat thickness (Fig. 4B). The reported microporosity of clays, regardless of texture and mineralogy, ranges from 15 % to 72 % (Table 2). The reported clay coat thickness is usually smaller than 30 μm (Worden et al., 2020; Li et al., 2024a). Therefore, the diffusion rate of silica across the coating layer may be decreased by up to four orders of magnitude compared to uncoated surface, given a maximum coat thickness of 30 μm (Figs. 4A–B).

4. Deceleration of the dissolution rate of detrital reactive grains being coated

4.1. Current knowledge: inspirations from coupled dissolution–precipitation reactions

4.1.1. Recognition of the impact of secondary coating layer on primary mineral dissolution

First, it is important to note that, to our knowledge, no studies have specifically investigated the influence of grain-coating clays on the dissolution rate of detrital reactive grains (e.g., feldspar) being coated. However, as a comparable process, we may obtain important inspirations from the coupled dissolution-precipitation reactions. The process involving the dissolution of a primary mineral (a parent mineral) with the concurrent precipitation of one or more secondary minerals or phases (product minerals formed through the alteration of the parent mineral) at the same spatial locality is termed coupled dissolution-

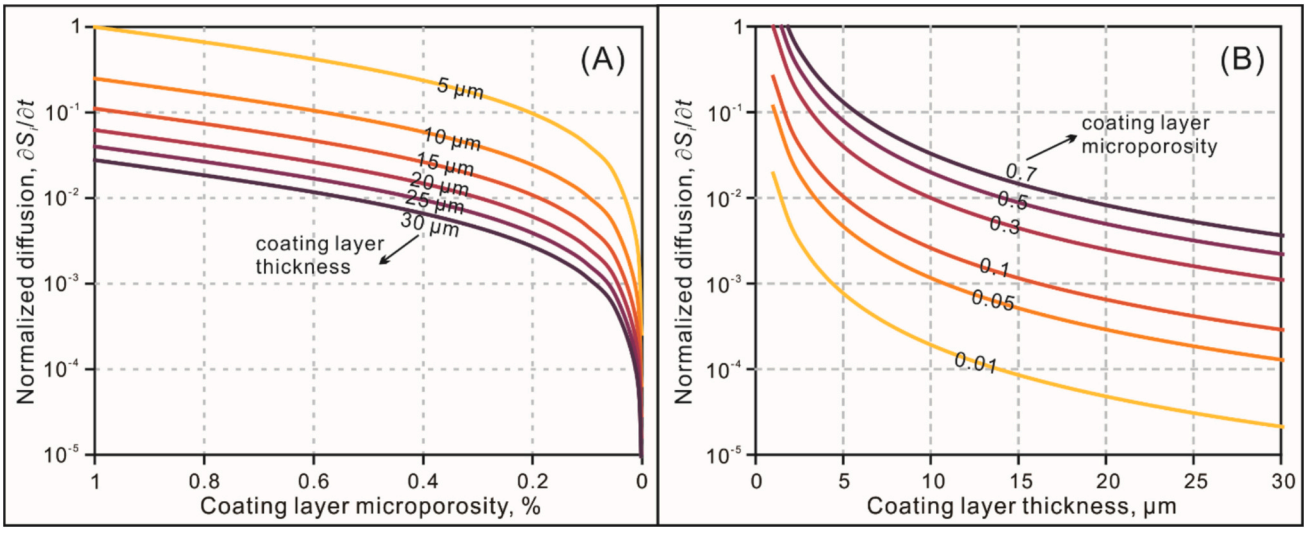

Fig. 4. Correlations between normalized diffusion ($\frac{\partial S_i}{\partial t}$) across the coating layer and the microporosity of the coating layer (A), as well as between normalized diffusion and the thickness of the coating layer (B) at 100 °C.

precipitation reactions (Putnis, 2009; Ruiz-Agudo et al., 2014; Altree-Williams et al., 2015). Secondary phases tend to nucleate and grow on the surface of primary minerals and thereby form a secondary layer that can passivate the surface of primary minerals (Ruiz-Agudo et al., 2014; Altree-Williams et al., 2015). The potential effects of secondary phases on the dissolution rate of the primary mineral during the coupled dissolution-precipitation process have been discussed in field observations, laboratory experiments and simulation studies. The observed effects of secondary phases on the dissolution rate of the primary mineral can be generally classified into three categories, including (1) retarding the dissolution rate of the primary mineral (Nugent et al., 1998; Daval et al., 2009; Zhu et al., 2010; Parruzot et al., 2015), (2) promoting the dissolution rate of the primary mineral (Murakami et al., 1998), and (3) negligibly affecting the dissolution rate of the primary mineral (Hodson, 2003; Stockmann et al., 2014). Although the mechanisms by which secondary phases affect the dissolution rate of the primary mineral are not well established at present, it is likely that they are collectively controlled by at least four factors.

Firstly, the precipitation of secondary phases on the surface of the primary mineral can passivate the surface of primary minerals and therefore reduce the accessible surface area of the primary mineral (Daval et al., 2009; Stockmann et al., 2014). Daval et al. (2009) suggested the following equation to account for the passivation of surface area of the primary mineral caused by secondary phases, assuming all secondary phases precipitated on the primary mineral surface:

$$SA_{(t)} = SSA_{(0)}\left[V_{primary(0)} - k_p\left(V_{secondary(t)}\right)^p\right] \quad (27)$$

where $SA_{(t)}$ is the surface area of primary mineral at time t, $SSA_{(0)}$ is the initial specific surface area of primary mineral, $V_{primary(0)}$ is the initial volume of primary mineral, $V_{secondary(t)}$ is the volume of secondary phase at time t, k_p is a proportionality factor, and p is a sphericity factor related to the grain shape.

Secondly, the secondary phases are typically porous, which may retard the diffusion of ions in free pore water passing through the coating secondary phases (see Section 3) and therefore affect the dissolution rate of the primary mineral (Altree-Williams et al., 2015; Emmanuel, 2022). Thirdly, the precipitation of secondary phases consumes a part of the elements released from primary minerals and serves as a sink for these elements. In this way, the precipitation of secondary minerals is able to alter the saturation index with respect to the primary mineral and therefore affect the dissolution rate of the primary mineral (Murakami et al., 1998; Parruzot et al., 2015). Fourthly, based on the third point, the precipitation rate of the secondary phase can determine the extent and rate of the change in saturation index with respect to primary minerals (Emmanuel and Ague, 2011; Altree-Williams et al., 2015). In this way, the precipitation rate of the secondary phase may affect the dissolution rate of the primary mineral.

These four factors have significant implications for evaluating the influence of grain-coating clays on the dissolution rates of detrital reactive grains being coated in sandstones. However, this work mainly discusses the influence of already-existing clay coats, while the new precipitation of clay coats is not the focus. Therefore, the potential influences from the afore-mentioned third and fourth factors in coupled dissolution-precipitation reactions will not be discussed.

4.1.2. An integrated diffusion boundary layer model

In the context of coupled dissolution-precipitation reactions, Emmanuel (2022) integrated the influence of coating secondary phases on the diffusion of ions (Eq. 23) into the dissolution rate of the primary mineral (Fig. 5). The coating layer was treated as an insoluble porous layer. The dissolution rate of the primary mineral was assumed to be exclusively dependent on the proton concentration and independent on the precipitation rate of secondary phase. Therefore, the diffusion of proton across the coating layer may serve as the rate-limiting step for the dissolution of the primary mineral. The reduction of the primary mineral dissolution rate was found to be correlated with three attributes of the coating layer, including the coating layer thickness (l), the porosity/tortuosity ratio (ε) of the coating layer, and the Biot number which denotes the ratio of the dissolution rate of the primary mineral to the diffusion of proton across the coating layer. It is important to note that the coating layer thickness shown in Fig. 5 is normalized to the thickness of the fluid boundary (water film) adjacent to a solid surface (Emmanuel, 2022), which is estimated to range from several micrometres to tens of micrometres (Emmanuel, 2022). Therefore, a normalized coating layer thickness (L) of 0–10 is equivalent to the actual coating layer thickness ranging from 0 to ~100 μm. It is demonstrated that a decreasing ε value, an increasing coating layer thickness, as well as an increasing Biot number can result in increased reduction of the dissolution rate of primary mineral (Figs. 5A–B).

However, it is important to note that the study of Emmanuel (2022) considers the dissolution rate of primary minerals to be exclusively dependent on the proton concentration. The passivation of the surface area of primary minerals, i.e., surface area reduction occupied by the coating layer, was not considered. Moreover, the study of Emmanuel (2022) only considers the full coat scenario (coat coverage = 100 %). The influence of discontinuous coating layer on the dissolution rate of detrital reactive grains being coated was not discussed.

4.2. Discussion: applying knowledge from coupled dissolution-precipitation reactions to clay coats

4.2.1. Reduction in the accessible surface area of detrital reactive grains

Section 2 has discussed the influence of grain-coating clays on the reduction of the accessible surface area of detrital grains (Figs. 2–3). It is likely that the typically observed grain-coating clays may reduce the accessible surface area of detrital reactive grains by up to one order of magnitude. In this way, the dissolution rate of detrital reactive grains may be reduced by up to one order of magnitude.

The method (Eq. 27) constructed by Daval et al. (2009) to account for the passivation (i.e., generation of secondary phases on primary mineral surface) of the primary mineral surface caused by the concurrent precipitation of secondary phases is not applicable for grain-coating clays. In fact, the Eq. 27 treats the secondary phases as nonporous materials (Daval et al., 2009). However, grain-coating clays are typically porous (Table 2; Figs. 1C–D). Moreover, it is likely that the coverage of the secondary phase is assumed to be linearly correlated with the volume of the secondary phase. In this way, the volume of secondary phase is directly employed in this equation. However, previous studies have indicated that clay coat volume is a function of grain size, coat coverage, and coat thickness (Li et al., 2024a). Therefore, clay coat volume may exhibit diverse relationships with coat coverage, including positive correlations (Wooldridge et al., 2018; Taylor et al., 2022; Aro et al., 2023), absence of statistical correlations (Bloch et al., 2002; Bello et al., 2021; Taylor et al., 2022), and even negative correlations (Bloch et al., 2002).

4.2.2. Reduction of diffusion and primary mineral dissolution rates

Section 3 has discussed the influence of grain-coating clays on retarding the diffusion rate of molecules and ions passing through the coating layer (Fig. 4). Given the reported microporosity of grain-coating clays ranging from 15 % to 72 % (Table 2) and the coat thickness of up to ~30 μm (Worden et al., 2020; Li et al., 2024a), the diffusion of ions and molecules across the coating layer may be retarded by up to four orders of magnitude compared to coat-free grains (Figs. 4A–B).

Regarding the diffusion boundary layer model constructed by Emmanuel (2022), the microporosity of grain-coating clays ranges from 15 % to 72 % (Table 2). The tortuosity (τ) can be estimated using Eq. 24 (see Section 3). Therefore, the ratio (ε) of porosity over tortuosity of the coating layer ranges from 0.068 to 0.559. The Biot numbers of aluminosilicate minerals are estimated to be very low (Emmanuel, 2022) and therefore have a minor influence on the dissolution rate of the primary

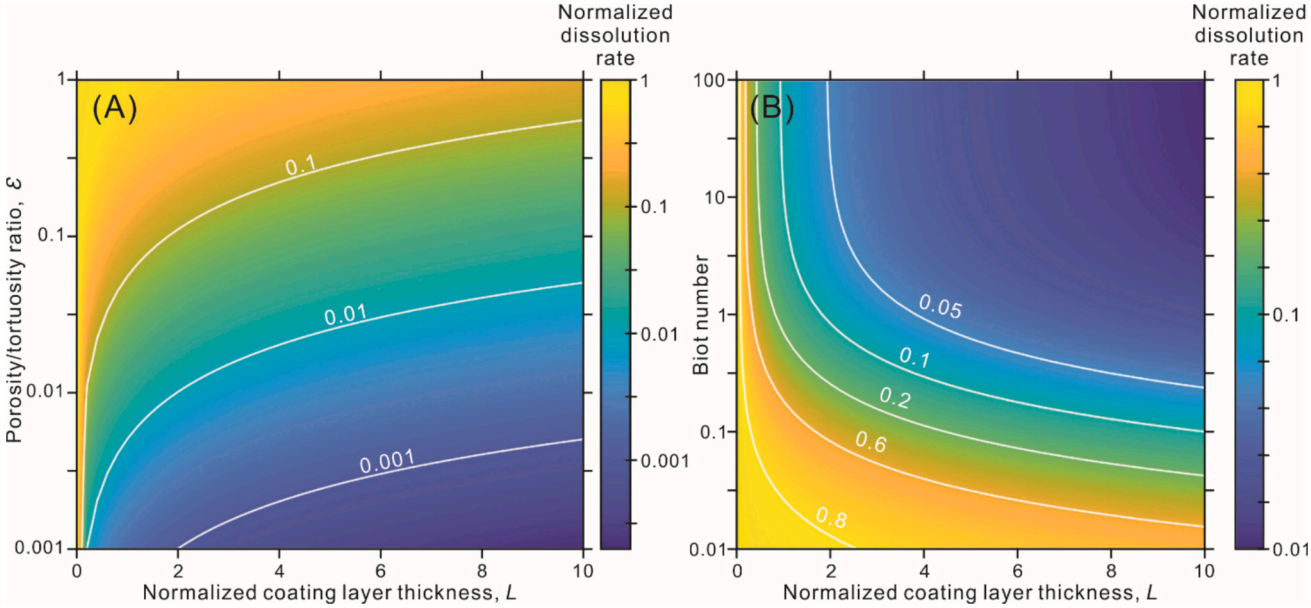

Fig. 5. (A) The reduction in the dissolution rate of the primary mineral correlates with the normalized coating layer thickness (L) and porosity/tortuosity ratio (ε) (Emmanuel, 2022); and (B) The reduction in the dissolution rate of the primary mineral correlates with the normalized coating layer thickness and the Biot number; the ε was set to 0.1.

mineral (Fig. 5B). For example, Emmanuel (2022) estimated the Biot numbers for forsterite and wollastonite, which are two relatively reactive silicate minerals, to be 1.1×10^{-5} and 0.031, respectively. Therefore, if Fig. 5A is used as a reference, the dissolution rate of detrital reactive minerals coated with clays, given the coat thickness of up to ~30 μm, can be maximumly scaled down by up to two orders of magnitude.

4.3. Discussion: influence on mineral dissolution and precipitation

In this section, we conducted reaction path models using the Geochemist's Workbench® Pro version 13.0 to discuss the influence of K-feldspar dissolution rate reduction caused by clay coats, as an example, on water-rock interactions in sandstones. The model construction, mineral dissolution and precipitation rate laws, kinetic parameter selection, and the method accounting for clay coat volume were mainly based on our earlier studies (Li et al., 2024a, 2024b). The inhibitive effect of clay coats on quartz cements was implemented using Eq. 2 (Lander and Walderhaug, 1999; Walderhaug et al., 2000). The detrital compositions in sandstones (arkose) are composed of 40 % quartz and 30 % K-feldspar. Kaolinite and chlorite were selected to be the grain-coating clays, representing a less reactive coating phase and a highly reactive coating phase, respectively. Grain size was set to 0.2 mm, representing fine sandstone. Clay coat coverage is set to 99 % (refers to Li et al., 2024a). Coat thickness was set to 10 μm. The temperature was set to 100 °C, which corresponds to the maximum concentration of dissolved organic acids in formation waters (Carothers and Kharaka, 1978; Lundegard and Kharaka, 1994; Kharaka and Hanor, 2014). The initial water compositions are in equilibrium with all primary minerals and refer to Table S1 for kaolinite coat cases and Table S2 for chlorite coat cases. The initial water compositions are in equilibrium with all minerals (pH = 6). 1000 mg/L acetic acid was injected to the system, while pH was set to 5 to facilitate mineral dissolution and precipitation (Tables S1 and S2). K-feldspar dissolution rate was artificially reduced by 0–2 orders of magnitude (Fig. 6).

It is illustrated that the amount of dissolved K-feldspar significantly decreases with decreasing K-feldspar dissolution rate in both cases (Figs. 6A and D). Petrographic data from Aro et al. (2023) exhibits a negative correlation ($R^2 = 0.52$) between coat coverage and secondary porosity in sandstones derived from feldspar dissolution in the Skagerrak Formation, North Sea, UK (Fig. S2A of Supplementary Material), which is likely consistent with this conclusion. However, it is important to note that the development of secondary porosity is simultaneously controlled by numerous factors, such as the supply of organic acids and CO_2, the sample location with respect to the sandstone-shale interface, and fluid flow velocity (Ehrenberg, 1991; Bjørlykke and Jahren, 2012; Yuan et al., 2017; Li et al., 2024b). These factors may result in the absence of significant statistical correlation between coat coverage and secondary porosity in other datasets (Fig. S2B of Supplementary Material; e.g., Busch et al., 2020; Monsees et al., 2021).

Moreover, the dissolution amounts of K-feldspar in the kaolinite coat case (Fig. 6A) are significantly higher than those in the chlorite coat case (Fig. 6D). This is due to the preferential dissolution of K-feldspar over kaolinite coat, as well as the preferential dissolution of chlorite coat over K-feldspar. As a result, in the kaolinite coat case, kaolinite exhibits only precipitation (Fig. 6B), while chlorite exhibits only dissolution in the chlorite coat case (Fig. 6E). The precipitation amounts of kaolinite and quartz in the kaolinite coat case also decrease with decreasing K-feldspar dissolution rate (Figs. 6B–C). In comparison, the dissolution amount of chlorite (Fig. 6E) and the precipitation amount of quartz (Fig. 6F) in the chlorite coat case are not significantly influenced by the reduction of K-feldspar dissolution rate. In other words, the influence of the reduction of the dissolution rate of detrital reactive grains on water-rock interactions in sandstones is simultaneously controlled by the reactivity of grain-coating clays, which is discussed in next section. However, it is important to note that these simulations are only theoretical investigations without validations from real samples. In fact, either preferential dissolution of detrital K-feldspar or chlorite coat may be observed in fields (see Section 5.4), depending on diverse geological-geochemical conditions in fields.

5. Potential dissolution of grain-coating clays

5.1. Current knowledge: challenges in identifying the dissolution of clay coats

To our understanding, grain-coating clay minerals are usually treated as a chemically-stable phase in the past evaluations of their roles

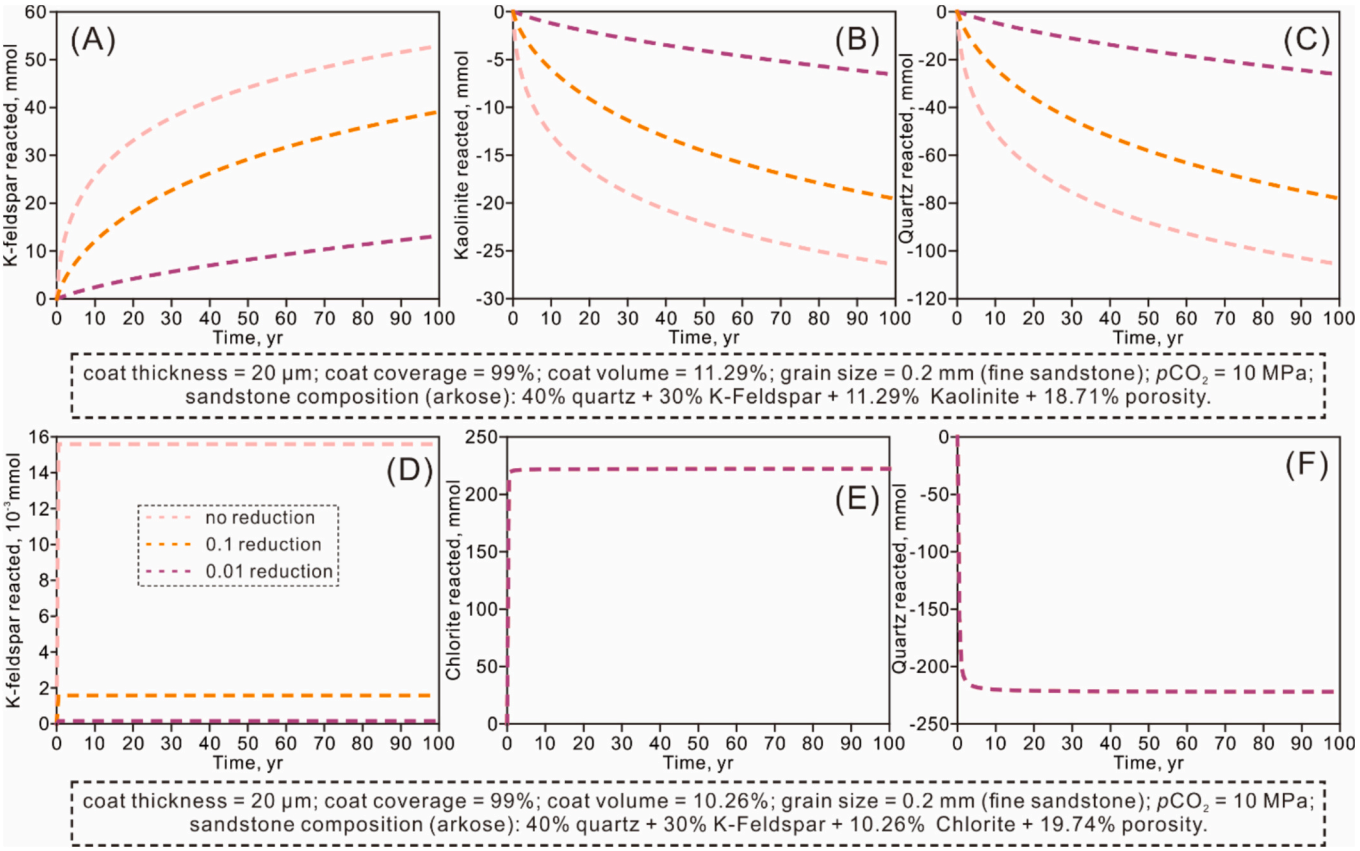

Fig. 6. Reaction path modelling results illustrating the changes in mineral dissolution (positive values) and precipitation (negative values) with the incorporation of different orders of magnitude of reduction in K-feldspar dissolution rate. (A–C) Kaolinite coat. (D—F) Chlorite coat.

in sandstones. In comparison, the alteration or dissolution of clay coats are rarely discussed. This may be mainly due to two aspects. Firstly, one single grain-coating clay platelet is typically very small with a platelet length (equivalent to coat thickness) of up to 30–50 μm (Worden et al., 2020; Li et al., 2024a) and a platelet thickness of smaller than 0.1–0.3 μm (Figs. 1C–D; Xia et al., 2020). Therefore, it might be difficult to identify the dissolution of clay coats in low-resolution images. More importantly, the dissolution of detrital reactive grains such as feldspars typically has remnant structures (e.g., Figs. 1E–F), which makes observers confidently confirm the dissolution of detrital reactive grains. In fact, high-resolution SEM images have illustrated that one single chlorite platelet becomes thinner from the detrital grain surface to the open pore space (Fig. 1D; Walderhaug and Porten, 2022). However, due to the lack of knowledge about the original crystal shape, it is difficult to confidently confirm whether or not this thinning characteristic is caused by the dissolution of clay coats. Secondly, petrographic observations have illustrated that feldspars being coated are dissolved whereas clay coats maintain original grain shape (e.g., Figs. 1E–F; Griffiths et al., 2021; Walderhaug and Porten, 2022; Li et al., 2023a). This may support the relatively chemically-stable property of clay coats.

In the following sections, we first reviewed the only two studies we found that have provided solid evidences supporting the dissolution of clay coats (Higgs et al., 2015; Waldmann and Gaupp, 2016). Subsequently, we discussed the potential influences of clay coat dissolution on sandstone porosity and the processes resulting in the preferential dissolution of either clay coats or detrital feldspar.

5.2. *Current knowledge: real cases describing the dissolution of grain-coating clays*

Higgs et al. (2015) reported the dissolution of grain-coating Fe-rich chlorite in natural CO_2 sandstone reservoirs from the Lower Cretaceous Pretty Hill Formation, Otway Basin, Australia (Fig. 7). Samples from four wells in four adjacent reservoirs were analysed (Fig. 7H), including Redman-1 (CO_2 < 0.1 mol%), Zema-1 (CO_2 < 0.3 mol%), Ladbroke Grove-3 (CO_2: 29.2–56.6 mol%), and Garvoc-1 (CO_2: 96.7 mol%). Moreover, all samples from Redman-1, Zema-1, and Garvoc-1 are located above gas-water-contact (GWC), whereas samples located at both above and below GWC in Ladbroke Grove-3 are collected. The mineralogy derived from both point-counting and Quantitative Evaluation of Materials by Scanning Electron Microscopy (QEMSCAN) methods has indicated that the samples from low CO_2 wells (Redman-1 and Zema-1) have significantly lower contents of grain-coating chlorite compared to samples from the moderate CO_2 well (Ladbroke Grove-3 and above GWC) and the high CO_2 well (Garvoc-1) (Figs. 7A and E). Furthermore, samples below the GWC of Ladbroke Grove-3 also have significantly higher volumes of chlorite than samples above the GWC (Figs. 7A and E). These differences support that the low volumes of chlorite in the moderate (Ladbroke Grove-3) and high CO_2 (Garvoc-1) wells result from the dissolution of pre-existing chlorite coats. As the by-products of chlorite dissolution, kaolinite (Figs. 7B and F), quartz overgrowth (Fig. 7C), and siderite (Figs. 7D and G) are higher in the moderate (Ladbroke Grove-3) and high CO_2 (Garvoc-1) wells. Therefore, the following three reactions were proposed to represent the dissolution of chlorite coats in the Pretty Hill Formation (Luquot et al., 2012; Higgs et al., 2015).

$$\begin{aligned} Fe_5Al_2Si_3O_{10}(OH)_8\ (\text{Daphnite}) + 10CO_2 + 3H_2O \rightarrow 5FeCO_3\ (\text{Siderite}) \\ + Al_2Si_2O_5(OH)_4\ (\text{Kaolinite}) \\ + SiO_2\ (\text{Quartz}) + 2H^+ + 5HCO_3{}^-{}_{(aq)} \end{aligned} \quad (28)$$

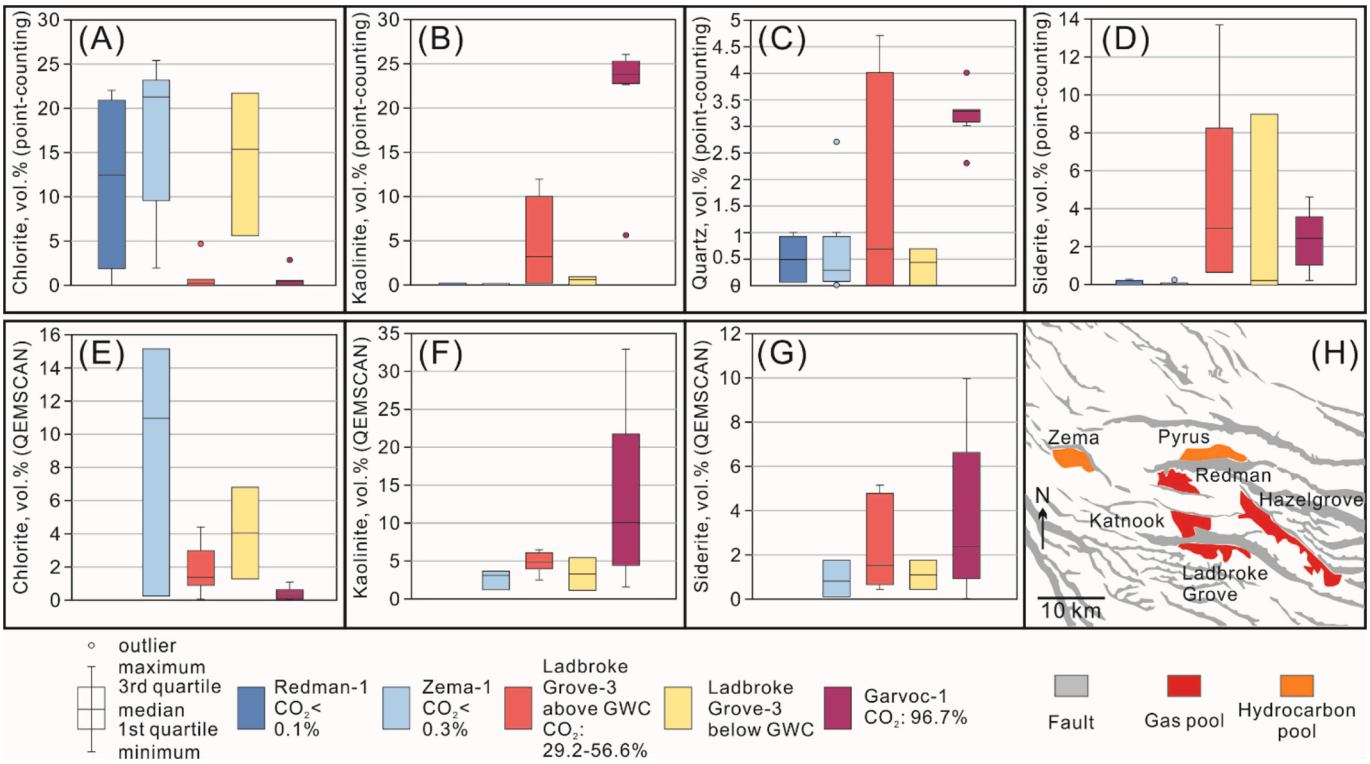

Fig. 7. (A–D) Point-counting mineral compositions in the Lower Cretaceous Pretty Hill Formation sandstones from different wells, Otway Basin, Australia. (E–G) QEMSCAN mineral compositions. (H) Well locations with the respective fluid compositions indicated. All data are derived from Higgs et al. (2015).

$$\begin{aligned}Fe_3Mg_2Al_2Si_3O_{10}(OH)_8\ (\text{Chamosite}) + 5CO_2 \rightarrow 3FeCO_3\ (\text{Siderite})\\ + 2MgCO_3\ (\text{Magnesite})\\ + Al_2Si_2O_5(OH)_4\ (\text{Kaolinite})\\ + SiO_2\ (\text{Quartz}) + 2H_2O\end{aligned} \quad (29)$$

$$\begin{aligned}Fe_3Mg_2Al_2Si_3O_{10}(OH)_8\ (\text{Chamosite}) + 3Ca^{2+}\\ + 6CO_2 \rightarrow 3CaFe(CO_3)_2\ (\text{Ankerite})\\ + Al_2Si_2O_5(OH)_4\ (\text{Kaolinite})\\ + SiO_2\ (\text{Quartz}) + H_2O + 2Mg^{2+} + 2H^+\end{aligned} \quad (30)$$

Waldmann and Gaupp (2016) investigated the origin of grain-rimming kaolinites (Figs. 8A–B) observed in the Permian, Rotliegend, natural gas filed sandstones, Southern Permian Basin, Northeast Netherlands. Waldmann and Gaupp (2016) suggested that the grain-rimming kaolinite resulted from the dissolution of pre-existing grain-rimming chlorite. They provided the following four main arguments to support this hypothesis: (1) Kaolinite generated through the dissolution of K-feldspar typically exhibits morphologies such as booklets, vermicular, or blocky (Hurst and Nadeau, 1995; Yuan et al., 2015; Li et al., 2023c); (2) Quantified K-feldspar dissolution (1.4–3.7 vol% in average) from thin sections is insufficient to generate kaolinite amounts comparable to the petrographic quantification (2.9–5.3 vol% in average); (3) Grain-coating chlorites, both Mg-rich and Fe-rich, have been reported in regions adjacent to the study area within the same basin (Gaupp et al., 1993; Hillier et al., 1996); and (4) Geochemical modelling involving chlorite dissolution induced by CO_2-charged fluids, both Mg-rich chlorite and Mg-Fe-rich chlorite, can produce kaolinite amounts comparable to petrographic quantifications (Figs. 8C–D).

The afore-mentioned two case studies (Higgs et al., 2015; Waldmann and Gaupp, 2016) provide strong supports for the dissolution of grain-coating chlorite by acidic waters charged with CO_2. They also probably highlight an in situ coupled dissolution-reprecipitation process. As a result, by-products of the dissolution of pre-existing chlorite coats, such as kaolinite (Figs. 8A–B), can still maintain grain-coating morphology. However, to our knowledge, no studies have reported the dissolution of other grain-coating clay minerals.

5.3. Discussion: potential influences on sandstone porosity

Although the afore-mentioned two cases studies well illustrated the dissolution of chlorite coats, the influence of the dissolution of chlorite coats on sandstone porosity was not discussed in both studies. The first major barrier is the difficulty in confidently and precisely identifying and quantifying the dissolution of chlorite coats. Secondly, regarding the cases of Higgs et al. (2015) and Waldmann and Gaupp (2016), the volumes of pre-existing chlorite coats are unknown and seem impossible to reconstruct. Thirdly, it is challenging to precisely identify and quantify the by-products exclusively from the dissolution of chlorite coats. Taking the case study of Higgs et al. (2015) as an example, in addition to chlorite, the dissolution of feldspars and laumontite can all produce kaolinite and quartz, making it difficult to precisely distinguish and quantify the kaolinite and quartz exclusively derived from the dissolution of chlorite coats.

$$\begin{aligned}Ca(Al_2Si_4O_{12})\cdot 4H_2O\ (\text{Laumontite}) + CO_2 \rightarrow CaCO_3\ (\text{Calcite})\\ + Al_2Si_2O_5(OH)_4\ (\text{Kaolinite})\\ + 2SiO_2\ (\text{Quartz}) + 2H_2O\end{aligned} \quad (31)$$

Nevertheless, we utilized Eq. 28 to provide a rough estimation of the net volume changes in this reaction involving the dissolution of chlorite and the precipitation of carbonates, kaolinite, and quartz. The molar volumes of minerals were derived from the dataset of Lawrence Livermore National Laboratory (LLNL; Bethke, 2008). The results indicate that the net volume change through Eq. 28 is 51.94 cm^3 per one mole of daphnite dissolution, suggesting a net porosity decrease. Moreover, Li

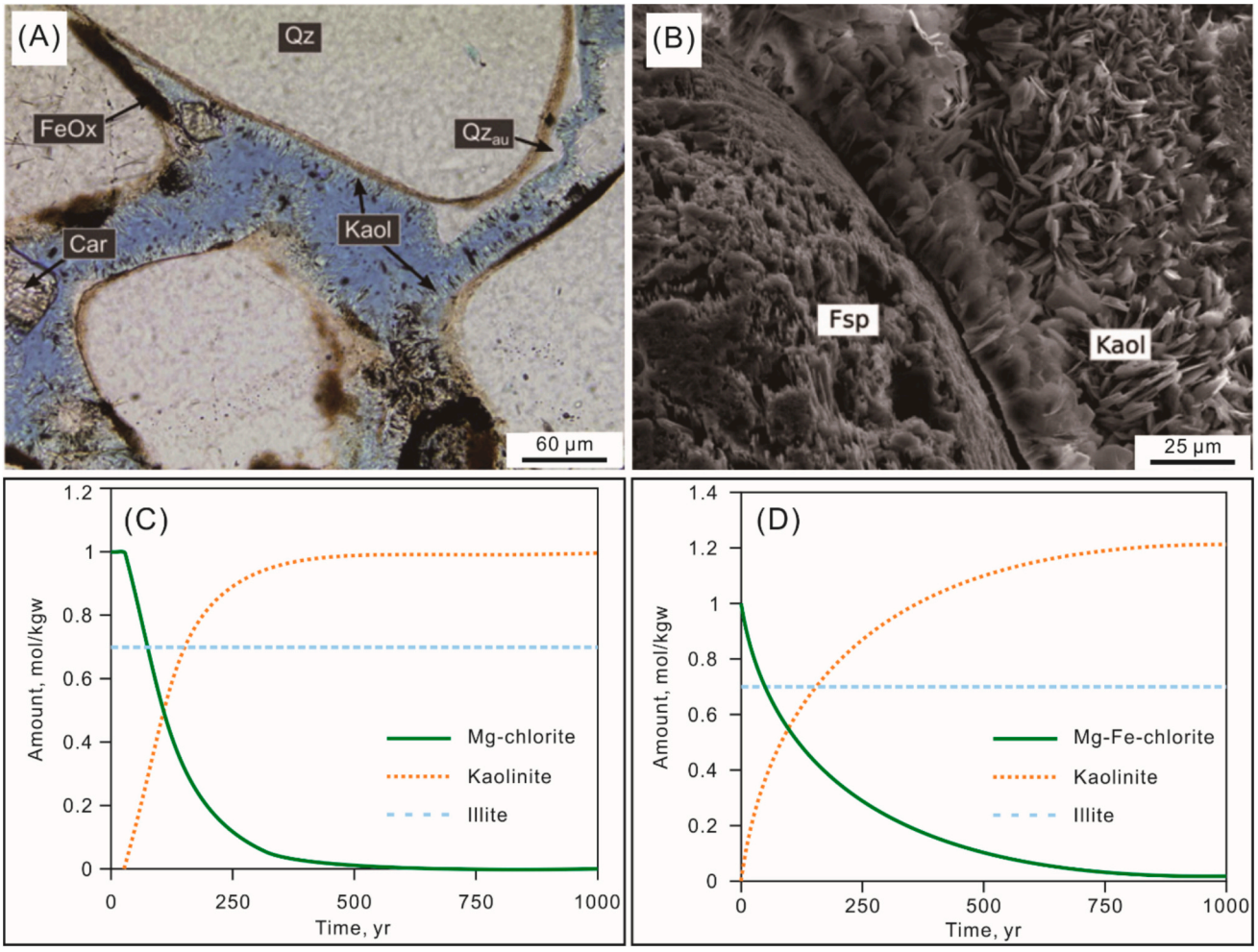

Fig. 8. (A–B) Thin section and SEM images showing grain-rimming kaolinite observed in the Permian Rotliegend natural gas filed sandstones, Southern Permian Basin, Northeast Netherlands (Waldmann and Gaupp, 2016). (C—D) Two geochemical modelling cases involving Mg-rich chlorite (C) and Mg-Fe-rich chlorite (D), respectively (Waldmann and Gaupp, 2016). CO_2 gas was injected into the system to induce mineral dissolution and precipitation. Car, carbonate; FeOx, Fe-oxide; Fsp, feldspar; Kaol, kaolinite; Qz, detrital quartz; Qz_{au}, authigenic quartz.

et al. (2024a) employed reactive transport modelling under variable petrographic and geochemical conditions to discuss the potential influence of the dissolution of chlorite coats on sandstone porosity. Both CO_2 and acetic acid were injected to induce mineral dissolution and precipitation, representing HCO_3^--rich and HCO_3^--depleted fluids (Li et al., 2024a). Reactive transport modelling results illustrate that sandstone porosity can be significantly decreased in the CO_2-charged fluid, which is mainly attributed to the precipitation of siderite and magnesite (Li et al., 2024a). In comparison, sandstone porosity can be slightly decreased in the acetic-acid-charged fluid, which is mainly attributed to the redistribution of kaolinite and quartz caused by fluid transport (Li et al., 2024a). However, a serious drawback of the study by Li et al. (2024a) is that it is not validated with real petrographic data.

5.4. *Discussion: origin of controversial petrographic observations*

Either the preferential dissolution of chlorite coats (Higgs et al., 2015; Waldmann and Gaupp, 2016) or detrital feldspar grains being coated (Figs. 1E–F; Griffiths et al., 2021; Walderhaug and Porten, 2022; Li et al., 2023a) have been reported. This discrepancy may result from multiple potential factors, such as water chemistry, accessible surface areas of grain-coating clays and detrital feldspars, and mineralogy of the grain-coating clays and detrital feldspars.

5.4.1. *Less reactive grain-coating clay minerals*

One likely cause for the preferential dissolution of detrital feldspars over grain-coating clays may be that the grain-coating clay is less reactive than detrital feldspar. For example, Fig. 6A and B have illustrated that K-feldspar being coated is dissolved while kaolinite coat is not. The preferential dissolution of K-feldspar over kaolinite is due to the dissolution rate of K-feldspar being greater than that of kaolinite.

5.4.2. *Substantially reduced accessible surface area of grain-coating clays*

Regarding the highly reactive grain-coating chlorite, one likely cause resulting in the preferential dissolution of detrital feldspars over chlorite coats may be due to the accessible surface area of chlorite coats has been substantially reduced. The potential significant reduction in the accessible surface area of grain-coating chlorite may be feasible because the chlorite platelets are closely stacked together, which may result in the occupation of part of the surface by each other (e.g., Fig. 1C). To explore the feasibility of such an effect, we conducted reaction path simulations with the Geochemist's Workbench® Pro version 13.0 involving K-feldspar, quartz, and grain-coating chlorite (Figs. 9A–D). The model setup, including mineral composition, water composition, kinetic rate laws, and the introduction of chlorite coat, refers to Li et al. (2024a). The initial water compositions are in equilibrium with all minerals (pH = 6; Table S2). An amount of 1000 mg/L of acetic acid was added to water compositions, while the pH was set to 5 to facilitate mineral dissolution

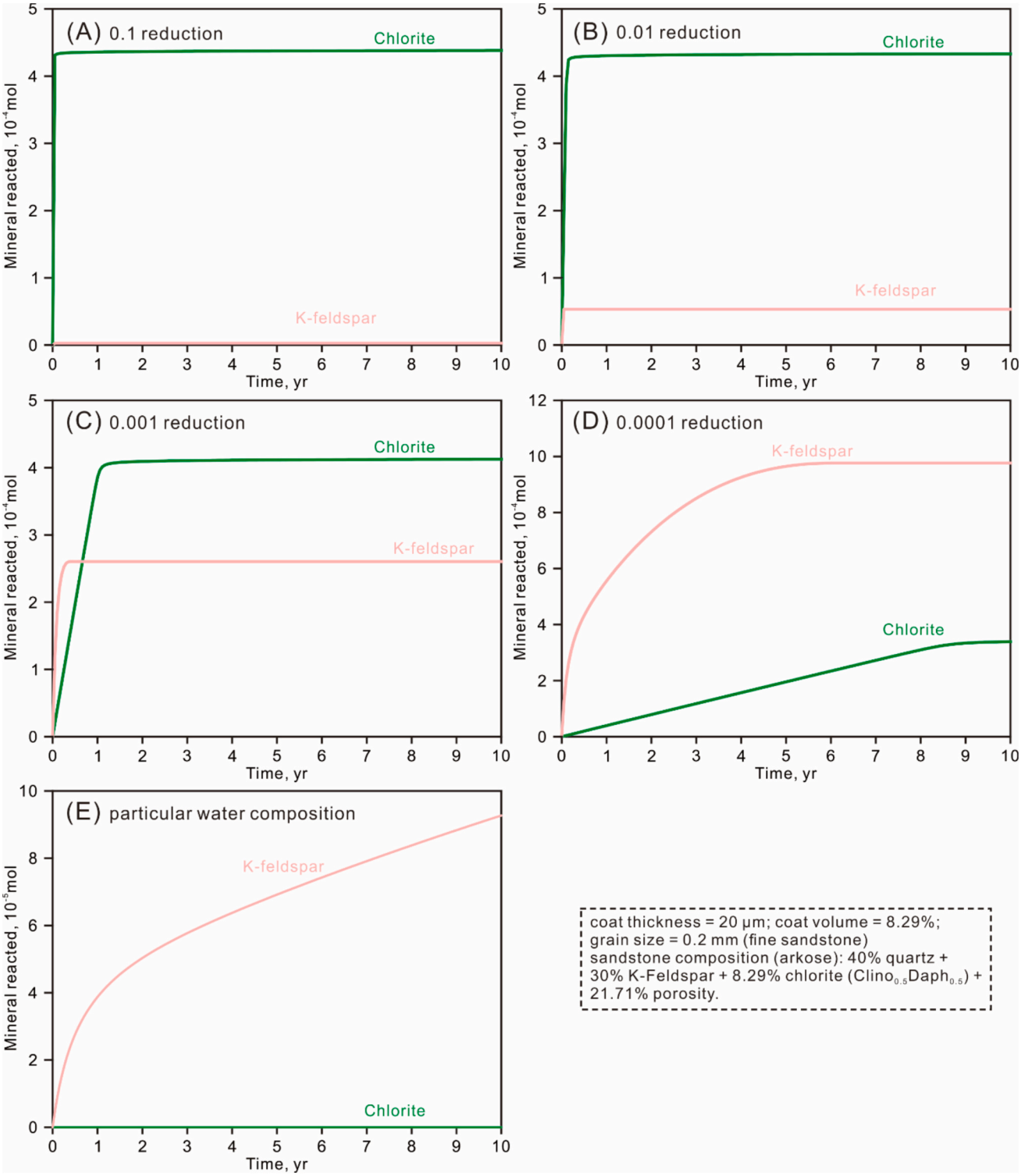

Fig. 9. Reaction path simulations illustrating the dissolution of K-feldspar and grain-coating chlorite. (A–D) The accessible surface area of chlorite was scaled down by 1–4 orders of magnitude, respectively. (E) A particular inflowing water, which is slightly supersaturated with respect to chlorite but slightly undersaturated with respect to K-feldspar, is employed.

and precipitation (Table S2). The initial accessible surface areas of K-feldspar and chlorite were set to 14.6 cm^2/g (Beckingham et al., 2016) and 280 cm^2/g (Domènech et al., 2002), respectively. Subsequently, the accessible surface area of chlorite was reduced by 1–4 orders of magnitude (Figs. 9A–D). It is illustrated that a minimum surface area scaling factor of 10^{-4} is required to derive the preferential dissolution of K-feldspar over chlorite in this case (Fig. 9D).

However, a key uncertainty is that, to our knowledge, no studies have experimentally measured the accessible surface area of grain-coating chlorite. Alternatively, Peters (2009) measured the accessibility (the proportion of surface area in contact with pore space) of kaolinite-coated sandstones. The value of accessible surface area of grain-coating kaolinite was not explicitly reported. Instead, Peters (2009) reported that 65–86 % of the total accessible surface area of the

sandstone samples originated from grain-coating kaolinite, while the remaining 14–35 % was derived from detrital grains. Thus, the total accessible surface area derived from grain-coating kaolinite is 1.86–6.14 times higher than that derived from detrital grains. Moreover, Waldmann et al. (2014) utilized a geometric method to estimate the accessible surface area of kaolinite-coated sandstones. The calculated accessible surface area of kaolinite coats is 1.58 m^2/g (volume = 4.1 %), while the accessible surface area of K-feldspar is 0.31 m^2/g (volume = 11.3 %). The calculated surface area of grain-coating kaolinite (1.58 m^2/g) is within one order of magnitude of the reported ranges of BET surface area of pure unconsolidated kaolinite (3.17–13.2 m^2/g; Beckingham et al., 2016) and high-resolution 2D SEM image-derived surface area of kaolinite in consolidated sandstones (13.2 m^2/g; Beckingham et al., 2016). Therefore, the total accessible surface area of kaolinite coat is 1.85 times higher than that of K-feldspar. In our simulations (Fig. 9D), the initial accessible surface area of chlorite coat is reduced to 0.028 cm^2/g. The initial total surface area provided by grain-coating chlorite, considering its initial volume, is 30.8 cm^2. The initial total surface area of K-feldspar, considering its initial volume, is 59,930 cm^2. Therefore, the total surface area of K-feldspar is about 2000 times higher than that of chlorite. Therefore, if we consider the findings of Peters (2009) and Waldmann et al. (2014) as references, a scaling factor of 10^{-4} used in Fig. 9D for explaining the significantly reduced dissolution rate of chlorite appears unlikely to be realistic in real samples.

5.4.3. Formation water compositions

The second likely cause for the preferential dissolution of detrital feldspar over chlorite coats may be attributed to the formation water compositions. In all the afore-mentioned numerical simulations, the initial water compositions are hypothesized to be in equilibrium with all minerals (Tables S1 and S3). However, previous studies have suggested that grain-coating chlorite mainly forms through either (1) the transformation of precursor clay coats such as smectite (Hillier, 1994; Beaufort et al., 2015; Worden et al., 2020) or (2) direct precipitation from chlorite-supersaturated pore waters (Worden et al., 2020; Charlaftis et al., 2021; Haile et al., 2022). Both pathways require that the formation water compositions are supersaturated with respect to chlorite. Therefore, it is possible that, following the inflow of acidic waters, the formation water compositions remain supersaturated with respect to chlorite while becoming undersaturated with respect to K-feldspar.

To investigate the feasibility of such an effect, we conducted additional reaction path simulations using the Geochemist's Workbench® Pro version 13.0 (Fig. 9E). The model setup, including mineral composition, kinetic rate laws, and the introduction of chlorite coat, refers Li et al. (2024a). The initial water composition was originally derived from the study of Li et al. (2024a) (Table S2), which is in equilibrium with all minerals ($\log(Q/K) = 0$). The initial water pH was 6 (Table S2). Subsequently, we artificially increased the Mg^{2+} concentration from 92.44 mg/kg to 600 mg/kg (Table S2), which resulted in supersaturation with respect to chlorite ($\log(Q/K) = 1.999$). This Mg^{2+} concentration (600 mg/kg) still falls within the range of reported Mg^{2+} concentrations in sedimentary basins (Palandri and Reed, 2001; Blondes et al., 2018; Li et al., 2023b). 1000 mg/L of acetic acid was added to induce mineral dissolution and precipitation, while the pH was adjusted to 5.8 (Table S2). The resulting water composition still remains slightly supersaturated with respect to chlorite ($\log(Q/K) = 0.205$), but is slightly undersaturated with respect to K-feldspar ($\log(Q/K) = -0.0534$). This resulting water composition was used to react with minerals (Fig. 9E). As expected, the inflowing water results in the preferential dissolution of K-feldspar over chlorite (Fig. 9E). However, this hypothesis requires validations through the evaluation of real formation water samples from chlorite-coated sandstone reservoirs.

6. Inhibition of quartz cements by grain-coating clays

6.1. Current knowledge

The overall precipitation rate of quartz cements can be constrained based on the Arrhenius equation (Walderhaug et al., 2000; Lander et al., 2008):

$$Rate = ASA \times 9 \times 10^{-12} \times e^{\frac{-E_a}{RT}} \times \left(1 - \left(\frac{Q}{K}\right)^m\right)^n \quad (32)$$

where Q and K are activity product and equilibrium constant, respectively, and m and n are empirical and dimensionless orders of the rate law.

This approach has been employed in the typical sandstone diagenesis simulator, Touchstone™, and has been validated by petrographic data from multiple case studies in different basins (Lander et al., 2008; Taylor et al., 2015; Busch et al., 2018). On the basis of this equation, the reduction of accessible surface area of detrital quartz caused by clay coats (Section 2) and the retard of silica diffusion passing through the coating layer (Section 3) may serve as two factors that decelerate the overall precipitation rate of quartz. However, one significant consideration is that the overall precipitation rate of quartz is only a temporal concept, focusing on the dimensionless growth speed of quartz. A significant drawback is that it does not account for the spatial factor, i.e., the crystallographic habit of quartz. In order to take the spatial factor into consideration, there are another two factors that need to be considered, including (1) the size of the gap between neighbouring clay platelets and (2) the solid barrier created by clay platelets themselves.

6.2. Discussion: the impact of gap size on constraining the size of quartz cements grown at gaps

6.2.1. Small gap size constrains tiny quartz crystal size

The sizes of quartz crystals grown at gaps between neighbouring clay platelets are typically very tiny, even if the samples have been exposed to high temperatures (Table 3). To understand the factors causing the tiny sizes of these quartz crystals, it is necessary to highlight the hydrothermal experiments conducted by Lander et al. (2008). The hydrothermal experiments were conducted at 300 °C and 69 MPa to examine the growth habits of alpha quartz overgrowths on a quartz plate (cut from a large quartz crystal) (Figs. 10A–I). Their study illustrated that the quartz growth rate (represented by secondary quartz length along crystallographic c axis) in a site with a smaller size was significantly smaller than that in a site with a greater size (Figs. 10A–C). The gaps and breaks in clay coats (Figs. 1A–D) are analogous to the different site sizes utilized in the hydrothermal experiments conducted by Lander et al. (2008), where either tiny or large quartz crystals were observed (Figs. 1A–D). Therefore, the hydrothermal experiments effectively reproduced two important petrographic observations. Firstly, tiny quartz crystals develop within gaps between individual clay platelets but fail to grow larger (Figs. 1C–D). Second, large quartz overgrowths are typically observed only at coat breaks with sizes exceeding ~10 μm (Figs. 1A–B; Table 4; Ajdukiewicz and Larese, 2012; Walderhaug and Porten, 2022).

However, a key question is why these tiny quartz crystals grown at gaps (Figs. 1C–D) fail to grow larger. To address this question, we must first highlight two phenomena illustrated by the hydrothermal experiments conducted by Lander et al. (2008). Firstly, quartz growth rates significantly decline (by an order of 20) after reaching euhedral (marked by red arrows in Fig. 10A). Secondly, quartz growth rates before reaching euhedral in all three sites with different sizes (represented by the slopes before arriving at red arrow points) are basically identical (Fig. 10A). Therefore, it can be concluded that smaller site sizes can only develop smaller quartz crystals mainly because quartz crystals grown at smaller site sizes reach euhedral faster than quartz crystals grown at

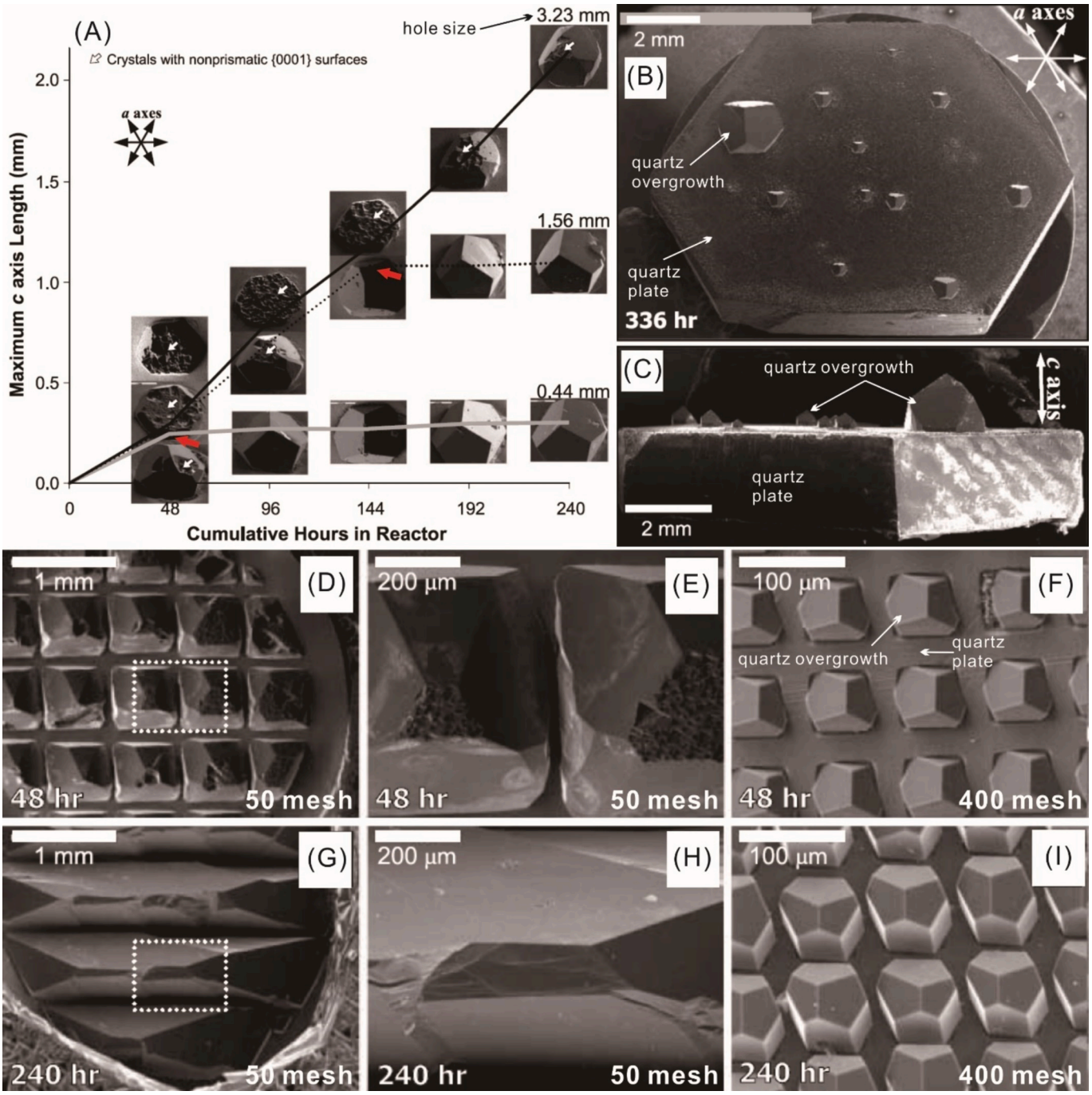

Fig. 10. (A–I) Hydrothermal experiments showing quartz growth habits on a quartz plate cut from a large quartz crystal (modified after Lander et al., 2008). (A) Correlation between the hydrothermal growth time and the maximum quartz growth length along crystallographic *c* axis in three artificial holes with different diameters (0.44 mm, 1.56 mm, and 3.23 mm) on the original quartz plate. (B—C) SEM images showing the plan view and side view of quartz overgrowths at holes with different diameters after 336 h. (D—I) Quartz growth habits on a plate covered with copper grids (indicated by where there is no quartz outgrowth).

greater site sizes (Lander et al., 2008).

This conclusion is consistent with the petrographic observations from Makowitz and Sibley (2001), who measured the quartz overgrowth thickness (not volume) and the grain radius of the host detrital quartz. They observed positive statistical correlations between overgrowth thickness and detrital quartz grain radius. This suggests that smaller detrital quartz grains can only develop thinner quartz overgrowths. Additionally, this conclusion can partially explain why detrital polycrystalline quartz grains in sandstones, compared to monocrystalline quartz grains, typically only develop thinner quartz overgrowths, as observed by Worden and Morad (2000), even if sandstones have been buried to very deep depths (Lander et al., 2008). This is due to polycrystalline quartz grains are typically composed of multiple microquartz crystals that can only provide smaller surface sites compared to monocrystalline quartz grains (Lander et al., 2008).

6.2.2. *Higher solubility of tiny quartz crystals constrains their further growth*

However, a significant issue arises from the hydrothermal experiments, as they indicate that the quartz growth rate after reaching euhedral only significantly declines but does not cease (Fig. 10A; Lander et al., 2008). In Table 3, we compiled data from clay-coated sandstones

Table 4
Reported clay-coated sandstones in which quartz overgrowth was observed at coat breaks.

Location	Age	Formation	Sedimentary environment	Depth (m)	T (°C)	Grain coating mineralogy	Coat break size (μm)	Quartz overgrowth at coat break	References
East China Sea Shelf	Oligocene	Xihu Fm.	Braided river delta	3799.4	146	Chlorite	~10	✓	Li et al. (2023a)
Norwegian continental shelf	Middle Jurassic	Garn Fm.	Shallow marine	4206.5	134	Chlorite	~35	✓	Walderhaug and Porten (2022)
	Upper Jurassic	Draupne Fm.	Turbiditic	4302.3	138	Microcrystalline quartz	~30	✓	
Norwegian continental shelf	Jurassic	Tilje Fm.	Shallow marine	5944.5	–	Chlorite	~15	✓	Griffiths et al. (2021)
North Sea	Triassic	Skagerrak Fm.	Fluvial	3548	140	Chlorite	~20	✓	Stricker and Jones (2018)
Petrel Gas Field, Australia	–	–	–	3587	–	Chlorite	~15	✓	Saïag et al. (2016)
North Sea	Jurassic	Fulmar Fm.	Shallow marine	5200	165	Detrital clay	~30	✓	Taylor et al. (2015)
Mobile Bay, Alabama	Jurassic	Norphlet Fm.	Eolian	6600–7000	–	Chlorite	~40	✓	Taylor et al. (2010)
Pakistani Sawan gas field	Cretaceous	Lower Goru Fm.	Shallow marine deltaic	3407.2	164	Chlorite	~50	✓	Berger et al. (2009)
Haltenbanken area	–	–	–	5101	–	Chlorite	–	✓	Bloch et al. (2002)
Norwegian continental shelf	Lower Jurassic	Tilje Fm.	Tidal shoreline	4619	–	Chlorite	~100	✓	Ehrenberg (1993)
	Upper-Lower Jurassic	Statfjord Fm.	Transgressive marine	3075	–	Chlorite	~30	✓	
	Lower Jurassic	Intra-Dunlin	Near shore shallow marine	4253	–	Chlorite	~10	✓	

where microquartz was observed beneath clay coats or in between single clay crystals. Notably, some of these samples have been buried to very high temperatures, reaching 160–180 °C (Table 3). Therefore, a critical question is why the tiny quartz cannot outgrow larger, especially in the samples that have experienced such high thermal exposure.

To address this, Jahren and Ramm (2000) and Walderhaug and Porten (2022) provided a geochemical explanation, by quoting the Ostwald-Freundlich equation (Eq. 33) which relates the rate of crystal growth with factors such as surface energy and saturation concentration.

$$S_c = S_0 exp\left(\frac{2V_m\gamma}{\nu RTr}\right) \quad (33)$$

where S_c is the solubility of a small quartz crystal, S_0 is the solubility of a quartz crystal of infinite size, V_m is the molar volume of quartz, γ is mineral-water interfacial free energy, ν is the moles of silica produced by the dissolution of one mole of quartz, R is universal gas constant, T is temperature in Kelvin, r is the site size radius.

The S_c/S_0 represents the ratio of the solubility of a small quartz crystal to that of a very large quartz crystal with an infinite size. This ratio serves as an indicator of the supersaturation levels required for the precipitation of small and large quartz crystals. Walderhaug and Porten (2022) calculated the S_c/S_0 ratios for three different site size radii, including 0.50 μm, 0.25 μm, and 0.10 μm. The calculated S_c/S_0 ratios for these radii are 1.008, 1.020 and 1.040, respectively. These values indicate that the solubility of a small quartz crystal is higher than that of a large quartz crystal. Similarly, Jahren and Ramm (2000) established a negative correlation, based on Eq. 33, between quartz crystal size and silica solubility. In simple terms, small quartz crystals are more soluble than large ones. Therefore, the growth of small quartz crystals may require a higher silica supersaturation than that required for large quartz crystals (Jahren and Ramm, 2000; Walderhaug and Porten, 2022).

In summary, three factors hinder the growth of tiny quartz crystals within gaps between individual clay platelets. Firstly, the gap size, which is determined by the texture of the clay coat, causes the tiny quartz crystals to reach euhedral faster. Once they reach euhedral, their growth rate significantly declines. Subsequently, the continued growth of these tiny quartz crystals requires a higher silica supersaturation and therefore fails to grow larger.

6.3. *Discussion: the impact of clay platelet barrier on preventing the coalescence of quartz crystals*

The hydrothermal experiments conducted by Lander et al. (2008) illustrated that neighbouring tiny quartz crystals, initially separated by a 50-mesh copper foil grid, ultimately coalesced after 240 h (Figs. 10D–E and G–H). In contrast, neighbouring tiny quartz crystals, initially separated by a 400-mesh copper foil grid, did not coalesce within the same timeframe (Figs. 10F and I). The 50-mesh grid results in a hole length (equivalent to site size) of 438 μm and a bar size of 62 μm (Lander et al., 2008). The 400-mesh grid results in a hole length of 62 μm and a bar size of 20 μm. This suggests that tiny quartz crystals grown on a surface characterized by a large hole/bar ratio were able to coalesce within a given time, while those grown on a surface characterized by a small hole/bar ratio were not.

Different from the copper foil grid used in the hydrothermal experiments, clay coats, such as chlorite coats, typically have a crystal platelet thickness smaller than 0.3 μm (Xia et al., 2020). In comparison, the gap size in between individual clay platelets can be as high as 7 μm (Walderhaug and Porten, 2022). Therefore, the gap/platelet thickness ratio, analogous to the hole/bar ratio in the hydrothermal experiments (Lander et al., 2008), may be high. Therefore, only considering the hole/bar ratio may not fully explain why clay coats prevent the coalescence of neighbouring quartz crystals. Instead, the presence of clay platelets physically stands in between two neighbouring tiny quartz crystals. If the height of an individual clay crystal exceeds the height of the tiny quartz crystals (Figs. 1C–D), this clay platelet can physically separate and prevent the potential connection of two neighbouring tiny quartz crystals. This diminishes the likelihood of neighbouring quartz crystals coalescing into larger crystals.

Theoretically, there might exist a threshold clay platelet height determining the efficiency in inhibiting the coalescence of neighbouring quartz crystals. However, grain-coating clays typically observed in natural environments have heights (equivalent to coat thickness) greater than 1 μm (Worden et al., 2020; Li et al., 2024a). In comparison, the observed tiny quartz crystals in between clay platelets are usually smaller than 0.1 μm (e.g., Figs. 1C–D; Walderhaug and Porten, 2022). Therefore, it can be concluded that typically observed grain-coating clays are effective in inhibiting the coalescence of neighbouring quartz crystals. This may also explain why very thin clay coating (a few

micrometres) can be as effective as coats thicker than 10 μm. However, if the height of a tiny quartz crystal exceeds the clay platelet height, it is possible that two neighbouring quartz crystals can connect outside the clay platelets (Figs. 1A–B). This scenario is more likely feasible for two neighbouring coat breaks (Figs. 1A–B). In summary, the physical barrier formed by clay platelets blocks the potential coalescence of neighbouring tiny quartz crystals and therefore prevents the continuing growth of tiny quartz crystals.

7. Perspectives and conclusions

Throughout this review the diverse roles of grain-coating clays in water-rock interactions in sandstones have been emphasized. This study, for the first time, integrated the multiple influences of clay coats on mineral dissolution and precipitation in sandstones, including their roles in reducing the surface area of detrital grains, retarding the diffusion of molecules and ions passing through the coating layer, decelerating the dissolution rate of detrital reactive grains being coated, and inhibiting the precipitation of quartz cements, and the influences of their dissolution. However, there is still a substantial room for improving our understanding of clay coats.

Firstly, although this study employed a geometric method to estimate the mathematical relationship between the reduction of surface area of detrital grains and coat parameters, experimental measurements are required to validate and correct the proposed mathematical relationship. A potentially feasible way is to employ high-resolution 2D SEM images and/or 3D micro-CT images segmented into pores and grains based on grey scales and integrated with mathematical algorithm to calculate the surface area of clay coats and detrital grains being coated.

Secondly, the mechanisms how the grain-coating clays decelerate the dissolution rate of reactive grains being coated requires validations. This should be based on the experimental evaluation of surface area of detrital reactive grains being coated. Subsequently, steady-state or flow-through dissolution experiments may be conducted to determine the dissolution rates of minerals and relate them with coat parameters. Such reactive transport experiments are representations of most natural geochemical settings and will highlight the role of transport on the dissolution and coating kinetics. It is important to note that highly reactive grain-coating clays (e.g., chlorite) may be preferentially dissolved prior to the dissolution of detrital grains being coated. Therefore, it might be appropriate to conduct the dissolution experiments using less reactive kaolinite coat. Thirdly, more petrographic data is required to discover whether the dissolution of clay coats is prevalent in different geological-geochemical conditions. Hence, reactive transport experiments, using naturally existing rock samples with varying mineral composition, can be conducted to understand different geological-geochemical field conditions. Only by overcoming these significant gaps can a true understanding of the roles of clay coats be achieved.

Declaration of competing interest

The authors declare that they have no known competing financial interests or personal relationships that could have appeared to influence the work reported in this paper.

Acknowledgements

We are deeply grateful for the invaluable comments and suggestions from the Editor and reviewers, and we also express our heartfelt gratitude to Dr. Robert Lander for his insightful discussions and valuable contributions to this topic. Dr. Huan Li acknowledges the financial supports provided by the Melbourne Research Scholarship (No. 396349) and the David Lachlan Hay Memorial Fund and many generous friends who financially supported him when he did not have income.

Appendix A. Supplementary data

Supplementary data to this article can be found online at https://doi.org/10.1016/j.earscirev.2025.105073.

Data availability

All data used has been provided.

References

Aagaard, P., Jahren, J.S., Harstad, A.O., Nilsen, O., Ramm, M., 2000. Formation of grain-coating chlorite in sandstones. Laboratory synthesized vs. natural occurrences. Clay Miner. 35, 261–269. https://doi.org/10.1180/000985500546639.

Ajdukiewicz, J.M., Lander, R.H., 2010. Sandstone reservoir quality prediction: the state of the art. AAPG Bull. 94, 1083–1091. https://doi.org/10.1306/intro060110.

Ajdukiewicz, J.M., Larese, R.E., 2012. How clay grain coats inhibit quartz cement and preserve porosity in deeply buried sandstones: Observations and experiments. AAPG Bull. 96, 2091–2119. https://doi.org/10.1306/02211211075.

Akinlotan, O.O., Moghalu, O.A., Hatter, S.J., Jolly, B.A., Anyiam, O.A., 2024. Paleoclimatic controls on clay mineral distribution in the early cretaceous (Barremian): the Wessex Basin, Southeast England. J. Earth Sci. 35, 2050–2066. https://doi.org/10.1007/s12583-023-1917-y.

Alansari, A., Salim, A.M.A., Janjuhah, H.T., Rahman, A.H.B.A., Fello, N.M., 2019. Quantification of clay mineral microporosity and its application to water saturation and effective porosity estimation: a case study from Upper Ordovician reservoir, Libya. J. Nat. Gas Geosci. 4, 139–150. https://doi.org/10.1016/j.jnggs.2019.04.005.

Altree-Williams, A., Pring, A., Ngothai, Y., Brugger, J., 2015. Textural and compositional complexities resulting from coupled dissolution–reprecipitation reactions in geomaterials. Earth Sci. Rev. 150, 628–651. https://doi.org/10.1016/j.earscirev.2015.08.013.

Anjos, S.M.C., De Ros, L.F., Silva, C.M.A., 2003. Chlorite authigenesis and porosity preservation in the Upper cretaceous marine sandstones of the Santos Basin, Offshore Eastern Brazil. In: Worden, R.H., Morad, S. (Eds.), Clay Mineral Cements in Sandstones, vol. 34. International Association of Sedimentologists Special Publication, pp. 291–316. https://doi.org/10.1002/9781444304336.ch13.

Aro, O.E., Jones, S.J., Meadows, N.S., Gluyas, J., Charlaftis, D., 2023. The importance of facies, grain size and clay content in controlling fluvial reservoir quality – an example from the Triassic Skagerrak Formation, Central North Sea, UK. Pet. Geosci. 29, 1–31. https://doi.org/10.1144/petgeo2022-043.

Azzam, F., Blaise, T., Dewla, M., Patrier, P., Beaufort, D., Elmola, A.A., Brigaud, B., Portier, E., Barbarand, J., Clerc, S., 2023. Role of depositional environment on clay coat distribution in deeply buried turbidite sandstones: Insights from the Agat field, Norwegian North Sea. Mar. Pet. Geol. 155, 106379. https://doi.org/10.1016/j.marpetgeo.2023.106379.

Bahlis, A.B., De Ros, L.F., 2013. Origin and impact of authigenic chlorite in the Upper cretaceous sandstone reservoirs of the Santos Basin, eastern Brazil. Pet. Geosci. 19, 185–199. https://doi.org/10.1144/petgeo2011-007.

Bartier, D., Buatier, M., Lopez, M., Potdevin, J.L., Chamley, H., Arostegui, J., 1998. Lithological control on the occurrence of chlorite in the diagenetic Wealden complex of the Bilbao anticlinorium (Basco-Cantabrian Basin, Northern Spain). Clay Miner. 33, 317–332. https://doi.org/10.1180/claymin.1998.033.2.13.

Beaufort, D., Rigault, C., Billon, S., Billault, V., Inoue, A., Patrier, P., 2015. Chlorite and chloritization processes through mixed-layer mineral series in low-temperature geological systems – a review. Clay Miner. 50, 497–523. https://doi.org/10.1180/claymin.2015.050.4.06.

Beckingham, L.E., Mitnick, E.H., Steefel, C.I., Zhang, S., Voltolini, M., Swift, A.M., Yang, L., Cole, D.R., Sheets, J.M., Ajo-Franklin, J.B., Depaolo, D.J., Mito, S., Xue, Z. Q., 2016. Evaluation of mineral reactive surface area estimates for prediction of reactivity of a multi-mineral sediment. Geochim. Cosmochim. Acta 188, 310–329. https://doi.org/10.1016/j.gca.2016.05.040.

Beckingham, L.E., Steefel, C.I., Swift, A.M., Voltolini, M., Yang, L., Anovitz, L.M., Sheets, J.M., Cole, D.R., Kneafsey, T.J., Mitnick, E.H., Zhang, S., Landrot, G., Ajo-Franklin, J.B., DePaolo, D.J., Mito, S., Xue, Z., 2017. Evaluation of accessible mineral surface areas for improved prediction of mineral reaction rates in porous media. Geochim. Cosmochim. Acta 205, 31–49. https://doi.org/10.1016/j.gca.2017.02.006.

Bello, A.M., Jones, S., Gluyas, J., Acikalin, S., Cartigny, M., 2021. Role played by clay content in controlling reservoir quality of submarine fan system, Forties Sandstone Member, Central Graben, North Sea. Mar. Pet. Geol. 128, 105058. https://doi.org/10.1016/j.marpetgeo.2021.105058.

Bello, A.M., AI-Ramadan, K., Babalola, L.O., Alqubalee, A., Amao, A.O., 2023. Impact of grain-coating illite in preventing quartz cementation: example from permo-carboniferous sandstone, Central Saudi Arabia. Mar. Pet. Geol. 149, 106073. https://doi.org/10.1016/j.marpetgeo.2022.106073.

Berger, A., Gier, S., Krois, P., 2009. Porosity-preserving chlorite cements in shallow-marine volcaniclastic sandstones: evidence from cretaceous sandstones of the Sawan gas field, Pakistan. AAPG Bull. 93, 595–615. https://doi.org/10.1306/01300908096.

Bethke, C.M., 2008. Geochemical and Biogeochemical Reaction Modelling, 2nd edition. Cambridge University Press, Cambridge. https://doi.org/10.1017/CBO9780511619670.

Billault, V., Beaufort, D., Baronnet, A., Lacharpagne, J.C., 2003. A nanopetrographic and textural study of grain-coating chlorites in sandstone reservoirs. Clay Miner. 38, 315–328. https://doi.org/10.1180/0009855033830098.

Bjørlykke, K., Jahren, J., 2012. Open or closed geochemical systems during diagenesis in sedimentary basins: Constraints on mass transfer during diagenesis and the prediction of porosity in sandstone and carbonate reservoirs. AAPG Bull. 96, 2193–2214. https://doi.org/10.1306/04301211139.

Bloch, S., Lander, R.H., Bonnell, L., 2002. Anomalously high porosity and permeability in deeply buried sandstone reservoirs: origin and predictability. AAPG Bull. 86, 301–328. https://doi.org/10.1306/61EEDABC-173E-11D7-8645000102C1865D.

Blondes, M.S., Gans, K.D., Engle, M.A., Kharaka, Y.K., Reidy, M.E., Saraswathula, V., Thordsen, J.J., Rowan, E.L., Morrissey, E.A., 2018. U.S. Geological Survey National Produced Waters Geochemical Database (ver. 2.3, January 2018). U.S. Geological Survey data Release. https://doi.org/10.5066/F7J964W8.

Boudreau, B.P., 1996. The diffusive tortuosity of fine-grained unlithified sediments. Geochim. Cosmochim. Acta 60, 3139–3142. https://doi.org/10.1016/0016-7037(96)00158-5.

Boudreau, B.P., 1997. Diagenetic Models and their Implementation: Modelling Transport and Reactions in Aquatic Sediments. Springer-Verlag, Berlin.

Brady, P.V., Walther, J.V., 1990. Kinetics of quartz dissolution at low temperatures. Chem. Geol. 82, 253–264. https://doi.org/10.1016/0009-2541(90)90084-K.

Busch, B., Hilgers, C., Lander, R.H., Bonnell, L.M., Adelmann, D., 2018. Reservoir quality and burial model evaluation by kinetic quartz and illite cementation modeling: Case study of Rotliegendes, North Germany. AAPG Bull. 102, 293–307. https://doi.org/10.1306/0503171605217075.

Busch, B., Hilgers, C., Adelmann, D., 2020. Reservoir quality controls on Rotliegend fluvio-aeolian wells in Germany and the Netherlands, Southern Permian Basin – Impact of grain coatings and cements. Mar. Pet. Geol. 112, 104075. https://doi.org/10.1016/j.marpetgeo.2019.104075.

Carothers, W.W., Kharaka, Y.K., 1978. Aliphatic acid anions in oil-field waters-implications for origin of natural gas. AAPG Bull. 62, 2441–2453. https://doi.org/10.1306/C1EA5521-16C9-11D7-8645000102C1865D.

Cecil, C.B., Heald, M.T., 1971. Experimental investigation of the effects of grain coatings on quartz growth. J. Sediment. Res. 41, 582–584. https://doi.org/10.1306/74D722E3-2B21-11D7-8648000102C1865D.

Charlaftis, D., Jones, S.J., Dobson, K.J., Crouch, J., Acikalin, S., 2021. Experimental study of chlorite authigenesis and influence on porosity maintenance in sandstones. J. Sediment. Res. 91, 197–212. https://doi.org/10.2110/jsr.2020.122.

Charlaftis, D., Jones, S.J., Grimm, L., Kappler, A., 2023. Interdependence between bacterial EPS and early grain coat development. Terra Nova 35, 241–249. https://doi.org/10.1111/ter.12648.

Daval, D., Martinez, I., Corvisier, J., Findling, N., Goffé, B., Guyot, F., 2009. Carbonation of Ca-bearing silicates, the case of wollastonite: Experimental investigations and kinetic modeling. Chem. Geol. 265, 63–78. https://doi.org/10.1016/j.chemgeo.2009.01.022.

Domènech, C., de Pablo, J., Ayora, C., 2002. Oxidative dissolution of pyritic sludge from the Aznalcóllar mine (SW Spain). Chem. Geol. 190, 339–353. https://doi.org/10.1016/S0009-2541(02)00124-9.

Dong, T., Gao, J., Li, S., et al., 2024. Quartz cementation in the lower Paleozoic shales, Middle Yangtze region, South China: Implications for shale reservoir properties. J. Earth Sci. 35, 1918–1933. https://doi.org/10.1007/s12583-023-1945-7.

Dowey, P.J., Hodgson, D.M., Worden, R.H., 2012. Pre-requisites, processes, and prediction of chlorite grain coatings in petroleum reservoirs: a review of subsurface examples. Mar. Pet. Geol. 32, 63–75. https://doi.org/10.1016/j.marpetgeo.2011.11.007.

Duteil, T., Bourillot, R., Grégoire, B., Virolle, M., Brigaud, B., Nouet, J., Braissant, O., Portier, E., Féniès, H., Patrier, P., Gontier, E., Svahn, I., Visscher, P.T., 2020. Experimental formation of clay-coated sand grains using diatom biofilm exopolymers. Geology 48, 1012–1017. https://doi.org/10.1130/G47418.1.

Ehrenberg, S.N., 1991. Kaolinized, potassium-leached zones at the contacts of the Garn Formation, Haltenbanken, mid-Norwegian continental shelf. Mar. Pet. Geol. 8, 250–269. https://doi.org/10.1016/0264-8172(91)90080-K.

Ehrenberg, S.N., 1993. Preservation of anomalously high porosity in deeply buried sandstones by grain-coating chlorite: examples from the Norwegian continental shelf. AAPG Bull. 77, 1260–1286. https://doi.org/10.1306/BDFF8E5C-1718-11D7-8645000102C1865D.

Emmanuel, S., 2022. Modeling the effect of mineral armoring on the rates of coupled dissolution-precipitation reactions: Implications for chemical weathering. Chem. Geol. 601, 120868. https://doi.org/10.1016/j.chemgeo.2022.120868.

Emmanuel, S., Ague, J.J., 2011. Impact of nano-size weathering products on the dissolution rates of primary minerals. Chem. Geol. 282, 11–18. https://doi.org/10.1016/j.chemgeo.2011.01.002.

Franks, S.G., Pantano, J., 2021. A simple, effective petrographic method for quantifying percent clay or other grain-coat coverage in sandstones. J. Sediment. Res. 91, 221–227. https://doi.org/10.2110/jsr.2020.135.

Freiburg, J.T., Amer, M., Henkel, K., Wemmer, K., Grathoff, G.H., 2022. Illitization in the Mt. Simon Sandstone, Illinois Basin, USA: Implications for carbon dioxide storage. Mar. Pet. Geol. 146, 105963. https://doi.org/10.1016/j.marpetgeo.2022.105963.

Gaupp, R., Matter, A., Platt, J., Ramseyer, K., Walzebuck, J., 1993. Diagenesis and fluid evolution of deeply buried Permian (Rotliegende) gas Reservoirs, Northwest Germany. AAPG Bull. 77, 1111–1128. https://doi.org/10.1306/BDFF8E0C-1718-11D7-8645000102C1865D.

Giannetta, L.G., Webb, N.D., Butler, S.K., Grigsby, N.P., 2021. Using clay microporosity to improve formation evaluation in potential residual oil zones: Cypress Sandstone, Illinois Basin. AAPG Bull. 105, 1595–1625. https://doi.org/10.1306/02262118214.

Gong, L., Gao, X., Qu, F., Zhang, Y., Zhang, G., Zhu, J., 2023. Reservoir quality and controlling mechanism of the Upper Paleogene fine-grained sandstones in lacustrine basin in the hinterlands of Northern Qaidam Basin, NW China. J. Earth Sci. 34, 806–823. https://doi.org/10.1007/s12583-022-1701-6.

Gould, K., Pe-Piper, G., Piper, D.J.W., 2010. Relationship of diagenetic chlorite rims to depositional facies in lower cretaceous reservoir sandstones of the Scotian Basin. Sedimentology 57, 587–610. https://doi.org/10.1111/j.1365-3091.2009.01106.x.

Griffiths, J., Worden, R.H., Wooldridge, L.J., Utley, J.E.P., Duller, R.A., 2018. Detrital clay coats, clay minerals, and pyrite: a modern shallow-core analogue for ancient and deeply buried estuarine sandstones. J. Sediment. Res. 88, 1205–1237. https://doi.org/10.2110/jsr.2018.56.

Griffiths, J., Worden, R.H., Utley, J.E.P., Brostrøm, C., Martinius, A.W., Lawan, A.Y., Al-Hajri, A.I., 2021. Origin and distribution of grain-coating and pore-filling chlorite in deltaic sandstones for reservoir quality assessment. Mar. Pet. Geol. 134, 105326. https://doi.org/10.1016/j.marpetgeo.2021.105326.

Haile, B.G., Hellevang, H., Aagaard, P., Jahren, J., 2015. Experimental nucleation and growth of smectite and chlorite coatings on clean feldspar and quartz grain surfaces. Mar. Pet. Geol. 68 (Part A), 664–674. https://doi.org/10.1016/j.marpetgeo.2015.02.006.

Haile, B.G., Hansen, H.N., Aagaard, P., Jahren, J., 2022. How do chlorite coatings form on quartz surface? J. Pet. Sci. Eng. 215 (Part B), 110682. https://doi.org/10.1016/j.petrol.2022.110682.

Hansen, H.N., Løvstad, K., Lageat, G., Clerc, S., Jahren, J., 2021. Chlorite coating patterns and reservoir quality in deep marine depositional systems – example from the cretaceous Agat Formation, Northern North Sea, Norway. Basin Res. 33, 2725–2744. https://doi.org/10.1111/bre.12581.

Heald, M.T., Anderegg, R.C., 1960. Differential cementation in the Tuscarora sandstone Virginia-West Virginia. J. Sediment. Res. 30, 568–577. https://doi.org/10.1306/74D70AA1-2B21-11D7-8648000102C1865D.

Heald, M.T., Larese, R.E., 1974. Influence of coatings on quartz cementation. J. Sediment. Res. 44, 1269–1274. https://doi.org/10.1306/212F6C94-2B24-11D7-8648000102C1865D.

Higgs, K.E., Haese, R.R., Golding, S.D., Schacht, U., Watson, M.N., 2015. The Pretty Hill Formation as a natural analogue for CO_2 storage: an investigation of mineralogical and isotopic changes associated with sandstones exposed to low, intermediate and high CO_2 concentrations over geological time. Chem. Geol. 399, 36–64. https://doi.org/10.1016/j.chemgeo.2014.10.019.

Hillier, S., 1994. Pore-lining chlorites in siliciclastic reservoir sandstones: electron microprobe, SEM and XRD data, and implications for their origin. Clay Miner. 29, 665–679. https://doi.org/10.1180/claymin.1994.029.4.20.

Hillier, S., Fallick, A.E., Matter, A., 1996. Origin of pore-lining chlorite in the aeolian Rotliegend of northern Germany. Clay Miner. 31, 153–171. https://doi.org/10.1180/claymin.1996.031.2.02.

Hodson, M.E., 2003. The influence of Fe-rich coatings on the dissolution of anorthite at pH 2.6. Geochim. Cosmochim. Acta 67, 3355–3363. https://doi.org/10.1016/S0016-7037(02)01370-4.

Hurst, A., Nadeau, P.H., 1995. Clay microporosity in reservoir sandstones: an application of quantitative electron microscopy in petrophysical evaluation. AAPG Bull. 79, 563–573. https://doi.org/10.1306/8D2B1598-171E-11D7-8645000102C1865D.

Jahren, J., Ramm, M., 2000. The porosity-preserving effects of microcrystalline quartz coatings in arenitic sandstones: Examples from the Norwegian Continental Shelf. In: Worden, R.H., Morad, S. (Eds.), Quartz Cementation in Sandstones, vol. 29. International Association of Sedimentologists Special Publication, pp. 271–280. https://doi.org/10.1002/9781444304237.ch18.

Kharaka, Y.K., Hanor, J.S., 2014. Deep fluids in sedimentary basins. In: Holland, H.D., Turekian, K.K. (Eds.), Treatise on Geochemistry, 2nd edition. Elsevier, Amsterdam, pp. 471–515. https://doi.org/10.1016/B978-0-08-095975-7.00516-7.

Lander, R.H., Walderhaug, O., 1999. Predicting porosity through simulating sandstone compaction and quartz cementation. AAPG Bull. 83, 433–449. https://doi.org/10.1306/00AA9BC4-1730-11D7-8645000102C1865D.

Lander, R.H., Larese, R.E., Bonnell, L.M., 2008. Toward more accurate quartz cement models: the importance of euhedral versus noneuhedral growth rates. AAPG Bull. 92, 1537–1563. https://doi.org/10.1306/07160808037.

Lander, R.H., Bonnell, L.M., Taylor, T.R., Espejo, I., 2022. Reservoir quality and diagenesis of Deepwater sandstones. In: Rotzien, J.R., Sears, R.A., Catuneanu, O., Yeilding, C.A., Hernández-Molina, F.J. (Eds.), Deepwater Sedimentary Systems. Elsiver, pp. 471–514. https://doi.org/10.1016/B978-0-323-91918-0.00011-6.

Landrot, G., Ajo-Franklin, J., Yang, L., Cabrini, S., Steefel, C.I., 2012. Measurement of accessible reactive surface area in a sandstone, with application to CO_2 mineralization. Chem. Geol. 318-319, 113–125. https://doi.org/10.1016/j.chemgeo.2012.05.010.

Lasaga, A.C., 1998. Kinetic Theory in the Earth Sciences. Princeton University Press, Princeton, NJ. https://doi.org/10.1515/9781400864874.

Lasaga, A.C., 2014. Kinetic Theory in the Earth Sciences. Princeton University Press, Princeton. https://doi.org/10.1515/9781400864874.

Li, H., Yang, X., Zhu, H., Wang, W., 2023a. Depositional and diagenetic controls on the evolution of abnormally high porosity in braided river deltaic sandstones (Oligocene), Xihu Depression, East China Sea. Geoenergy Sci. Eng. 226, 211751. https://doi.org/10.1016/j.geoen.2023.211751.

Li, H., Haese, R.R., Black, J.R., Du, X., Yang, X., Zhu, H., 2023b. The origin of two distinct diagenetic depth zones in hydrocarbon-bearing sediments of Huanghekou Sag, offshore Bohai Bay Basin, China. Mar. Pet. Geol., 106164 https://doi.org/10.1016/j.marpetgeo.2023.106164.

Li, H., Zhu, H., Du, X., Yang, X., 2023c. Secondary porosity generation in sandstones constrained by the fault movement, fluid flow, and mudstone–sandstone

interactions, offshore Bohai Bay Basin, China. AAPG Bull. 107, 785–821. https://doi.org/10.1306/09232220024.
Li, H., Hu, Q., Wang, F., Wang, M., Hao, Y., Wang, W., 2024a. Alteration of chlorite coats and sandstone porosity reduction: Insights from reactive transport modelling. Mar. Pet. Geol. 160, 106641. https://doi.org/10.1016/j.marpetgeo.2023.106642.
Li, H., Black, J.R., Hao, Y., Hao, P., Mishra, A., Haese, R.R., 2024b. Modelling diagenetic reactions and secondary porosity generation in sandstones controlled by the advection of low molecular weight organic acids. Basin Res. 36, e12860. https://doi.org/10.1111/bre.12860.
Li, Y.H., Gregory, S., 1974. Diffusion of ions in sea water and in deep-sea sediments. Geochim. Cosmochim. Acta 38, 703–714. https://doi.org/10.1016/0016-7037(74)90145-8.
Lin, J., Lin, C., Ma, P., Dong, C., Liu, B., Huang, X., Zhang, X., Zhao, X., 2023. The characteristics and origin of chlorite coats in the Oligocene gas sandstone reservoirs of the Upper Huagang Formation, Xihu Depression, East China Sea Shelf Basin. Sediment. Geol. 454, 106449. https://doi.org/10.1016/j.sedgeo.2023.106449.
Lundegard, P.D., Kharaka, Y.K., 1994. Distribution and occurrence of organic acids in subsurface waters. In: Pittman, E.D., Lewan, M.D. (Eds.), Organic Acids in Geological Processes. Springer-Verlag, Berlin, pp. 40–69. https://doi.org/10.1007/978-3-642-78356-2.
Luquot, L., Andreani, M., Gouze, P., Camps, P., 2012. CO_2 percolation experiment through chlorite/zeolite-rich sandstone (Pretty Hill Formation – Otway Basin–Australia). Chem. Geol. 294-295, 75–88. https://doi.org/10.1016/j.chemgeo.2011.11.018.
Makowitz, A., Sibley, D., 2001. Crystal growth mechanisms of quartz overgrowths in a Cambrian quartz qrenite. J. Sediment. Res. 71, 809–816. https://doi.org/10.1306/2DC4096A-0E47-11D7-8643000102C1865D.
Monsees, A.C., Busch, B., Hilgers, C., 2021. Compaction control on diagenesis and reservoir quality development in red bed sandstones: a case study of Permian Rotliegend sandstones. Int. J. Earth Sci. 110, 1683–1711. https://doi.org/10.1007/s00531-021-02036-6.
Morad, S., Al-Ramadan, K., Ketzer, J.M., De Ros, L.F., 2010. The impact of diagenesis on the heterogeneity of sandstone reservoirs: a review of the role of depositional facies and sequence stratigraphy. AAPG Bull. 94, 1267–1309. https://doi.org/10.1306/04211009178.
Murakami, T., Kogure, T., Kadohara, H., Ohnuki, T., 1998. Formation of secondary minerals and its effect on anorthite dissolution. Am. Minerl. 83, 1209–1219. https://doi.org/10.2138/am-1998-11-1209.
Nugent, M.A., Brantley, S.L., Pantano, C.G., Maurice, P.A., 1998. The influence of natural mineral coatings on feldspar weathering. Nature 395, 588–591. https://doi.org/10.1038/26951.
Oelkers, E.H., Bjørkum, P.A., Walderhaug, O., Nadeau, P.H., Murphy, W.M., 2000. Making diagenesis obey thermodynamics and kinetics: the case of quartz cementation in sandstones from offshore mid-Norway. Appl. Geochem. 15, 295–309. https://doi.org/10.1016/S0883-2927(99)00047-5.
Palandri, J.L., Reed, M.H., 2001. Reconstruction of *in situ* composition of sedimentary formation waters. Geochim. Cosmochim. Acta 65, 1741–1767. https://doi.org/10.1016/S0016-7037(01)00555-5.
Park, A.J., 2014. Water-rock interaction and reactive-transport modelling using elemental mass-balance approach: I. The methodology. Am. J. Sci. 314, 785–804. https://doi.org/10.2475/03.2014.02.
Parruzot, B., Jollivet, P., Rébiscoul, D., Gin, S., 2015. Long-term alteration of basaltic glass: Mechanisms and rates. Geochim. Cosmochim. Acta 154, 28–48. https://doi.org/10.1016/j.gca.2014.12.011.
Peters, C.A., 2009. Accessibilities of reactive minerals in consolidated sedimentary rock: an imaging study of three sandstones. Chem. Geol. 265, 198–208. https://doi.org/10.1016/j.chemgeo.2008.11.014.
Putnis, A., 2009. Mineral replacement reactions. Rev. Mineral. Geochem. 70, 87–124. https://doi.org/10.2138/rmg.2009.70.3.
Qin, F., Salek, M.F., Asadi, P., Iloejesi, C., Brunhoeber, O., Mahmood, M., Beckingham, L.E., 2023. Estimation of mineral accessible surface area from mineral abundance and clay content. ACS Earth Space Chem. 7, 326–337. https://doi.org/10.1021/acsearthspacechem.2c00181.
Ruiz-Agudo, E., Putnis, C.V., Putnis, A., 2014. Coupled dissolution and precipitation at mineral-fluid interfaces. Chem. Geol. 383, 132–146. https://doi.org/10.1016/j.chemgeo.2014.06.007.
Saïag, J., Brigaud, B., Portier, É., Desaubliaux, G., Bucherie, A., Miska, S., Pagel, M., 2016. Sedimentological control on the diagenesis and reservoir quality of tidal sandstones of the Upper Cape Hay Formation (Permian, Bonaparte Basin, Australia). Mar. Pet. Geol. 77, 597–624. https://doi.org/10.1016/j.marpetgeo.2016.07.002.
Schulz, H.D., Zabel, M., 2006. Marine geochemistry, second revised, updated and extended edition. Springer-Verlag, Heidelberg. https://doi.org/10.1007/3-540-32144-6.
Stockmann, G.J., Wolff-Boenisch, D., Bovet, N., Gislason, S.R., Oelkers, E.H., 2014. The role of silicate surfaces on calcite precipitation kinetics. Geochim. Cosmochim. Acta 135, 231–250. https://doi.org/10.1016/j.gca.2014.03.015.
Storvoll, V., Bjørlykke, K., Karlsen, D., Saigal, G., 2002. Porosity preservation in reservoir sandstones due to grain-coating illite: a study of the Jurassic Garn Formation from the Kristin and Lavrans fields, offshore Mid-Norway. Mar. Pet. Geol. 19, 767–781. https://doi.org/10.1016/S0264-8172(02)00035-1.
Stricker, S., Jones, S.J., 2018. Enhanced porosity preservation by pore fluid overpressure and chlorite grain coatings in the Triassic Skagerrak, Central Graben, North Sea, UK. Geol. Soc. Lond. Spec. Publ. 435, 321–341. https://doi.org/10.1144/SP435.4.
Tang, L., Gluyas, J., Jones, S., 2018. Porosity preservation due to grain coating illite/smectite: evidence from Buchan Formation (Upper Devonian) of the Ardmore Field, UK North Sea. Proc. Geol. Assoc. 129, 202–214. https://doi.org/10.1016/j.pgeola.2018.03.001.
Tartakovsky, D.M., Dentz, M., 2019. Diffusion in porous media: phenomena and mechanisms. Transp. Porous Media 130, 105–127. https://doi.org/10.1007/s11242-019-01262-6.
Taylor, T.R., Giles, M.R., Hathon, L.A., Diggs, T.N., Braunsdorf, N.R., Birbiglia, G.V., Kittridge, M.G., Macaulay, C.I., Espejo, I.S., 2010. Sandstone diagenesis and reservoir quality prediction: Models, myths, and reality. AAPG Bull. 94, 1093–1132. https://doi.org/10.1306/04211009123.
Taylor, T.R., Kittridge, M.G., Winefield, P., Bryndzia, L.T., Bonnell, L.M., 2015. Reservoir quality and rock properties modeling – Triassic and Jurassic sandstones, greater Shearwater area, UK Central North Sea. Mar. Pet. Geol. 65, 1–21. https://doi.org/10.1016/j.marpetgeo.2015.03.020.
Taylor, T.R., Lander, R.H., Bonnell, L.M., 2022. Sandstone petrography, petrology, and modelling. In: SEPM Concepts in Sedimentology and Paleontology, 13, pp. 1–356. https://doi.org/10.2110/sepmcsp.13.
Tester, J.W., Worley, W.G., Robinson, B.A., Grigsby, C.O., Feerer, J.L., 1994. Correlating quartz dissolution kinetics in pure water from 25 to 625°C. Geochim. Cosmochim. Acta 58, 2407–2420. https://doi.org/10.1016/0016-7037(94)90020-5.
Virolle, M., Brigaud, B., Beaufort, D., Patrier, P., Abdelrahman, E., Thomas, H., Portier, E., Samson, Y., Bourillot, R., Féniès, H., 2022. Authigenic berthierine and incipient chloritization in shallowly buried sandstone reservoirs: Key role of the source-to-sink context. Geol. Soc. Am. Bull. 134, 739–761. https://doi.org/10.1130/B35865.1.
Walderhaug, O., Porten, K.W., 2022. How do grain coats prevent formation of quartz overgrowths? J. Sediment. Res. 92, 988–1002. https://doi.org/10.2110/jsr.2021.049.
Walderhaug, O., Lander, R.H., Bjørkum, P.A., Oelkers, E.H., Bjørlykke, K., Nadeau, P.H., 2000. Modelling quartz cementation and porosity in reservoir sandstones: Examples from the Norwegian Continental Shelf. In: Worden, R.H., Morad, S. (Eds.), Quartz Cementation in Sandstones, vol. 29. International Association of Sedimentologists Special Publication, pp. 39–49. https://doi.org/10.1002/9781444304237.ch3.
Waldmann, S., Gaupp, R., 2016. Grain-rimming kaolinite in Permian Rotliegend reservoir rocks. Sediment. Geol. 335, 17–33. https://doi.org/10.1016/j.sedgeo.2016.01.016.
Waldmann, S., Busch, A., van Ojik, K., Gaupp, R., 2014. Importance of mineral surface areas in Rotliegend sandstones for modeling CO2–water–rock interactions. Chem. Geol. 378-379, 89–109. https://doi.org/10.1016/j.chemgeo.2014.03.014.
Wigley, M., Kampman, N., Dubacq, B., Bickle, M., 2012. Fluid-mineral reactions and trace metal mobilization in an exhumed natural CO_2 reservoir, Green River, Utah. Geology 40, 555–558. https://doi.org/10.1130/G32946.1.
Wooldridge, L.J., Worden, R.H., Griffiths, J., Thompson, A., Chung, P., 2017. Biofilm origin of clay-coated sand grains. Geology 45, 875–878. https://doi.org/10.1130/G39161.1.
Wooldridge, L.J., Worden, R.H., Griffiths, J., Utley, J.E.P., Thompson, A., 2018. The origin of clay-coated sand grains and sediment heterogeneity in tidal flats. Sediment. Geol. 373, 191–209. https://doi.org/10.1016/j.sedgeo.2018.06.004.
Wooldridge, L.J., Worden, R.H., Griffiths, J., Utley, J.E.P., 2019. Clay-coat diversity in marginal marine sediments. Sedimentology 66, 1118–1138. https://doi.org/10.1111/sed.12538.
Worden, R.H., Morad, S., 2000. Quartz cementation in oil field sandstones: A review of the key controversies. In: Worden, R.H., Morad, S. (Eds.), Quartz Cementation in Sandstones, vol. 29. International Association of Sedimentologists Special Publication, pp. 1–20. https://doi.org/10.1002/9781444304237.ch1.
Worden, R.H., Griffiths, J., Wooldridge, L.J., Utley, J.E.P., Lawan, A.Y., Muhammed, D.D., Simon, N., Armitage, P.J., 2020. Chlorite in sandstones. Earth Sci. Rev. 204, 103105. https://doi.org/10.1016/j.earscirev.2020.103105.
Xia, H., Perez, E.H., Dunn, T.L., 2020. The impact of grain-coating chlorite on the effective porosity of sandstones. Mar. Pet. Geol. 115, 104237. https://doi.org/10.1016/j.marpetgeo.2020.104237.
Xu, T., Apps, J.A., Pruess, K., Yamamoto, H., 2007. Numerical modeling of injection and mineral trapping of CO_2 with H_2S and SO_2 in a sandstone formation. Chem. Geol. 242, 319–346. https://doi.org/10.1016/j.chemgeo.2007.03.022.
Yuan, G.H., Cao, Y.C., Gluyas, J., Li, X.Y., Xi, K.L., Wang, Y.Z., Jia, Z.Z., Sun, P.P., Oxtoby, N.H., 2015. Feldspar dissolution, authigenic clays, and quartz cements in open and closed sandstone geochemical systems during diagenesis: typical examples from two sags in Bohai Bay Basin, East China. AAPG Bull. 99, 2121–2154. https://doi.org/10.1306/07101514004.
Yuan, G.H., Cao, Y.C., Gluyas, J., Jia, Z.Z., 2017. Reactive transport modeling of coupled feldspar dissolution and secondary mineral precipitation and its implication for diagenetic interaction in sandstones. Geochim. Cosmochim. Acta 207, 232–255. https://doi.org/10.1016/j.gca.2017.03.022.
Zalc, J.M., Reyes, S.C., Iglesia, E., 2004. The effects of diffusion mechanism and void structure on transport rates and tortuosity factors in complex porous structures. Chem. Eng. Sci. 59, 2947–2960. https://doi.org/10.1016/j.ces.2004.04.028.
Zerai, B., Saylor, B.Z., Matisoff, G., 2006. Computer simulation of CO_2 trapped through mineral precipitation in the Rose Run Sandstone, Ohio. Appl. Geochem. 21, 223–240. https://doi.org/10.1016/j.apgeochem.2005.11.002.
Zhu, C., Lu, P., Zheng, Z., Ganor, J., 2010. Coupled alkali feldspar dissolution and secondary mineral precipitation in batch systems: 4. Numerical modeling of kinetic reaction paths. Geochim. Cosmochim. Acta 74, 3963–3983. https://doi.org/10.1016/j.gca.2010.04.012.